REVIEW

Optical tomography of tissues

D.A. Zimnyakov, V.V. Tuchin

Abstract. **Methods of optical tomography of biological tissues are considered, which include pulse-modulation and frequency-modulation tomography, diffusion tomography with the use of cw radiation sources, optical coherent tomography, speckle-correlation tomography of nonstationary media, and optoacoustic tomography. The method for controlling the optical properties of tissues is studied from the point of view of increasing a probing depth in optical coherent tomography. The modern state and prospects of the development of optical tomography are discussed.**

1. Introduction

One of the fields of modern biomedical optics is the development of methods for probing biological tissues with radiation in the visible and near-IR regions to visualise their structure. Interest in such studies is caused by the following reasons:

(i) the development of safe methods for diagnostics of tissues; (ii) the outlook for imaging biological structures with a spatial resolution comparable with the wavelength of probe radiation; (iii) the possibility of multifunctional diagnostics of biological objects; and (iv) the existence of a unique transparency window of tissues in the spectral range between 650 and 1200 nm.

A combination of optical methods for visualisation of tissue structures, which are based on various effects of the interaction of light with scattering media, is called optical tomography. Compared to conventional methods (X-ray tomography, ultrasonic tomography, etc.), optical tomography is characterised by some special features. Among them is a variety of approaches for obtaining information on the object structure from the properties of detected radiation. At present, the optical tomography methods such as optical coherent tomography, modulation tomography, optical tomography of nonstationary media based on

speckle-correlation methods, etc. are being developed, as well as methods using the conversion of probe light to fields of other nature (for example, optoacoustic tomography). By comparing the principles of optical tomography and other methods for visualisation of tissue structures, note that there is no substantial difference in obtaining information on the object structure in these methods, which involves a series of successive measurements of the characteristics of transmitted or reflected probe radiation at different positions of a source and a detector.

The main problem of optical tomography is related to the properties of light propagating in tissues as inhomogeneous media with the inhomogeneity scale of the order of the wavelength of light. A light field transmitted through such an inhomogeneous object is characterised by a considerable excess of multiply scattered components over the non-scattered (ballistic) component. This complicates the application of conventional methods for reconstructing images by detecting the non-scattered component of radiation transmitted through an object (X-ray tomography) or reflected by the boundaries of layers with different wave impedances (ultrasonic tomography).

At present, two main trends in the development of optical tomography exist. The first one, which is called optical diffusion tomography, deals with the visualisation of large-scale objects (brain tomography, mammography) with the aim of detecting newgrowths (hematomas, tumors, etc.). The second trend is the morphological studies of relatively thin (~ 1 mm) tissue layers with the help of coherent and polarisation methods. The rapid development of this field during the last decade due to the advancement of optical coherent tomography and applications of this method in practice was stimulated by a low efficiency of methods of optical microscopy for studying tissue layers of thickness $0.5 - 1$ mm and thicker.

At the same time, optical diffusion tomography and tomography methods based on the detection of the ballistic component of transmitted radiation have the temporal and spatial resolutions that are insufficient for a morphological analysis of such objects. In addition, a standard optical coherent tomography system can be updated for endoscopic studies of real objects *in vivo*.

Concerning the development of optical diagnostic methods, note that biological tissues are characterised by intense scattering of light in the visible and near-IR regions, and in some cases, by selective absorption of light caused by the presence of natural chromophores in tissues (first of all, hemoglobin and melanin) [1–3]. Light in the visible region

D.A. Zimnyakov, V.V. Tuchin N.G. Chernyshevskii Saratov State University, ul. Moskovskaya 155, 410026 Saratov, Russia; e-mail: zimnykov@sgu.ssu.runnet.ru

is absorbed by hemoglobin. Melanin strongly absorbs light in the short-wavelength visible region, its absorption being gradually decreased with increasing wavelength. Scattering of light in biological tissues is caused by a spatial inhomogeneity of their structure at the cell and subcell levels, which is manifested in fluctuations δn of the refractive index. The components of the cellular structure of tissues such as cell membranes, cell nuclei, mitochondria, and other organelles, as well as melanin granules are considered as main scatterers of light.

The relation between the scatterer size and fluctuations δn results in anisotropic scattering of probe radiation. The degree of scattering anisotropy $g = \langle \cos \theta \rangle$, which is expressed in terms of the average value of the cosine of the scattering angle, is large, amounting to $0.65 - 0.9$ (predominantly forward scattering) and even to $0.96 - 0.98$ for some scatterers (erythrocytes) [4]. In most human tissues, scattering dominates over absorption outside the absorption bands (typical values of the scattering coefficient for soft tissues lie in the range from 10^2 to 10^4 cm^{-1}, while those of the absorption coefficient μ_a are $10^{-2} - 10$ cm^{-1}) [3].

Due to the absence of noticeable absorption in the spectral region between 0.65 and 1.2 μm, there exists the so-called transparency window, where the penetration depth of radiation into a tissue achieves $8 - 10$ mm. Fig. 1 illustrates the existence of the transparency window in biological tissues. Outside this window, the penetration depth is limited by absorption of IR radiation by water, which is one of the main components of tissues ($\lambda > 1.5$ μm) and absorption of the short-wavelength components of visible light by different chromophores, including water [3]. The existence of the transparency window favours the development of optical diagnostics because a variety of lasers are available emitting in this region.

In this review, we consider various methods of optical tomography using incoherent and coherent probe radiation.
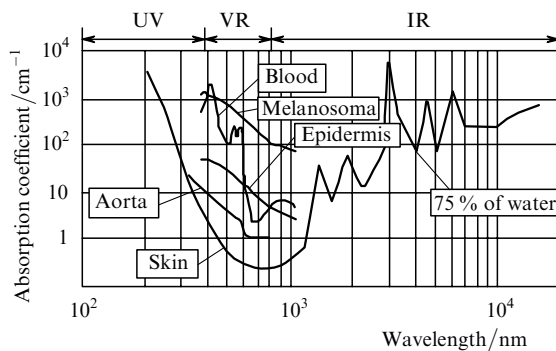
Figure 1. Absorption spectra of different tissues showing the transparency window in the visible (VR) and near-IR range.

2. Physical foundations of optical tomography

The propagation of light in biological tissues can be described by using the theory of radiation transfer in random media. There exist two approaches for the description of this phenomenon [5, 6]: the theory of radiation transfer, which considers the evolution of the energy flux of radiation propagating in a random medium, and the theory of multiple scattering, which describes the wave properties of scattered light fields in random media. Although, unlike the theory of multiple scattering, the theory of radiation transfer cannot describe interference effects upon scattering of coherent radiation, a fundamental interrelation exists between these two approaches, which is determined by the relation between the angular spectrum of the ray intensity, obtained within the framework of the radiation transfer theory, and the spatial correlation function of fluctuations of a scattered field, which is obtained in the theory of multiple scattering [6]. This interrelation allows one to introduce a universal characteristic for the description of light propagation in a random medium – the density $\rho(s)$ of distribution of the optical paths of components of the scattered field [7 – 10]. This universal characteristic makes it possible to obtain the parameters of the scattered field as the integral transformations of $\rho(s)$ with the corresponding kernels [7, 8, 11 – 13], while the function $\rho(s)$ can be obtained within the framework of the radiation transfer theory.

The most rigorous analysis of the propagation of light in a random medium involves the solution of a radiation transfer equation, whose scalar form, in the case of monochromatic light, is [5, 14]

$$\frac{s \nabla I(\boldsymbol{r}, \boldsymbol{s}, t)}{\mu_t} + t_f \frac{\partial I(\boldsymbol{r}, \boldsymbol{s}, t)}{\partial t} = -I(\boldsymbol{r}, \boldsymbol{s}, t) + \frac{\mu_s}{4\pi \mu_t}$$

$$\times \int_{4\pi} \left[\int_{4\pi}^{t} I(\boldsymbol{r}, \boldsymbol{s}', t) p(\boldsymbol{s}', t', \boldsymbol{s}, t) \mathrm{d}t' \right] \mathrm{d}\Omega + \frac{S(\boldsymbol{r}, \boldsymbol{s}, t)}{\mu_t}, \quad (1)$$

where $I(\boldsymbol{r}, \boldsymbol{s}, t)$ is the ray intensity of light scattered at the instant of time t at the point $\boldsymbol{r}$ in the direction $\boldsymbol{s}$; $p(\boldsymbol{s}', t', \boldsymbol{s}, t)$ is a time-dependent phase scattering function, which characterises the angular distribution of the radiation flux scattered by an elementary volume; Ω is the solid angle; $\mu_t = \mu_a + \mu_s$ is the extinction coefficient; $S(\boldsymbol{r}, t)$ is the source function; $t_f = I/\mu_t c$ is the characteristic time of radiation propagation in a medium between the successive events of interaction with local inhomogeneities; and c is the speed of light in a medium. In the general case, the solution of equation (1) with arbitrary boundary conditions in the analytic form is impossible. For this reason, Monte Carlo simulations of the photon transport in media are most convenient for analysis of radiation transfer in media with a complicated structure [15 – 17]. In the case of an adequately chosen scattering model, in particular, the phase function $p(\boldsymbol{s}', t', \boldsymbol{s}, t)$, the Monte Carlo simulations allow one to obtain an exact solution of the photon transport problem, whose macroscopic form corresponds to equation (1) with specified boundary conditions. This is used in verifying the validity of approximations of the radiation transfer equation, when the analytic solution is compared with Monte Carlo simulations [18, 19].

When the directed component $I(\boldsymbol{r}, \boldsymbol{s}, t)$ can be neglected compared to the isotropic component, equation (1) is transformed to the diffusion equation [5, 6]

$$\nabla \left(\frac{1}{3\mu_{tr}} \nabla U(\boldsymbol{r}, t) \right) - \mu_a U(\boldsymbol{r}, t) -$$

$$-\frac{1}{c}\frac{\partial U(\mathbf{r},t)}{\partial t} = -\frac{S_{\mathrm{d}}(\mathbf{r},t)}{3\mu_{\mathrm{tr}}}, \qquad (2)$$

where $U(\mathbf{r},t)$ is the diffusion component of the ray intensity; $\mu_{\mathrm{tr}} = \mu_{\mathrm{a}} + (1-g)\mu_{\mathrm{s}}$; and $S_{\mathrm{d}}(\mathbf{r},t)$ is the diffusion radiation source function.

The function $U(\mathbf{r},t)$, obtained by solving equation (2), is associated with the photon density at the point with coordinates $\mathbf{r}$ at the instant of time t, which is obtained by the Monte Carlo method. Outside a scattering medium, $U(\mathbf{r},t) = 0$. The condition of applicability of approximation (2) to the description of the intensity distribution of radiation scattered in a random medium can be formulated as $L \gg [(1-g)\mu_{\mathrm{s}}]^{-1}$, where L is the distance between a source and a detector. The parameter $l^* = (\mu'_{\mathrm{s}})^{-1} = [\mu_{\mathrm{s}}(1-g)]^{-1}$, which is called the transport length, plays an important role in the description of radiation transfer, by determining the path of a light beam in a medium at which a collimated light beam is transformed to diffuse radiation. Another condition of the applicability of the diffusion approximation is a weak absorption in a scattering medium, which is expressed by the condition $l^* \ll \mu_{\mathrm{a}}^{-1}$.

When these conditions are violated (for example, when radiation scattered near sources or radiation transmitted through a thin scattering layer with anisotropic scattering are detected), the diffusion approximation leads to substantial discrepancies with experimental data or Monte Carlo simulations ('the crisis of the diffusion approximation' takes place) [20, 21].

Despite these limitations, this approach can be applied to a number of problems of the propagation of light in biological objects (for example, in brain), which allows the use of the method for solving the boundary problems of diffusion and thermal conductivity in optical diffusion tomography. The solution of equation (2) for specified boundary conditions is related to the probability density $\rho(s)$. In the simplest case of an isotropic point source $I_0\delta(\mathbf{r})\delta(t')$ embedded into an infinite medium, when scattered radiation is detected with a point detector, the function $\rho(s)$ can be found from the Green function of equation (2) by making the substitution $s \to c(t - t')$.

To solve diffusion equation (2) for media with a restricted geometry, it is necessary to specify the boundary conditions and source functions taking into account the following restrictions [22–24].

(1) Upon probing a medium with a collimated light beam, a source of the diffusion component is localised not on the medium surface but at some depth $z_0 \sim l^*$, because the directed component is transformed to the diffusion one at the depth of the order of l^*. Therefore, the source function should have the form $I_0\delta(z - z_0)\varphi(x,y)\psi(t)$. It is also possible to use not a localised source but a source exponentially distributed over the depth, which corresponds to the transformation of the directed component to the diffusion one in a near-surface layer.

(2) The boundary condition for a classical diffusion problem is written as $U(\mathbf{r},t)|_{\mathbf{r}=\Omega} = 0$ (Ω is the boundary surface of a region where diffusion occurs). As applied to the diffusion of radiation, this condition should be modified to take into account the influence of reflection of light from the boundary. For example, in the case of diffusion of light in a semi-infinite medium, which is of interest for applications in diagnostics, when backscattered radiation is detected, this results in the boundary condition in the form $U(\mathbf{r},t)|_{z=-z_{\mathrm{p}}} = 0$ (z_{p} is the extrapolation length), i.e., the diffusion component vanishes not on the geometrical boundary but at some distance z_{p} from it. The ratio z_{p}/l^* depends on the reflectivity of the boundary.

The problem of diffusion of radiation in restricted regions can be solved using a standard method for solving boundary problems; for example, for regions representing a half-space or layers, the method of sources is used [9].

The influence of absorption on the transport properties of a scattering medium is an important question. The diffusion coefficient in the diffusion theory is $D = c/3[\mu_{\mathrm{a}} + (1-g)\mu_{\mathrm{s}}]$. At the same time, it was shown in papers [25–28] that the best agreement between the experiment and diffusion theory was achieved when D was assumed independent of μ_{a} (i.e., $D = c/3(1-g)\mu_{\mathrm{s}}$). This allows one to analyse the statistics of optical paths in an absorbing medium by calculating the probability density $\rho(s)$ for a non-absorbing medium with the specified values of μ_{s} and g, and then take into account absorption by introducing the Bouguer factor $\exp(-\mu_{\mathrm{s}}s)$ in the expression for $\rho(s)$.

A number of attempts have been made to modify the diffusion approximation and to use other methods for approximate solving equation (1) in order to obtain an analytic description of radiation transfer near the boundaries of a scattering medium, as well as in the cases of strong absorption and anisotropic scattering. Some results were obtained using the P_N approximation [29] based on the representation of the radiation flux in a medium expanded in spherical functions to take into account the scattering anisotropy (the diffusion approximation is equivalent to the P_1 approximation).

The radiation transfer described by a three-dimensional telegraph equation was considered in paper [30]. According to this approach, the derivative $\partial^2 U(\mathbf{r},t)/\partial t^2$ in the right-hand side of this equation takes into account the evolution of the ballistic component because the behaviour of the solution of the telegraph equation at small space–time scales is similar to that of the wave equation. At large times and distances, the solution of the telegraph equation tends asymptotically to that of equation (2).

The presence of regions with the values of μ_{a} and μ_{s} different from the average values in a scattering volume results in the difference of the function $\tilde{U}(\mathbf{r},t)$ and, hence, the probability density of optical paths $\tilde{\rho}(s)$ from $U(\mathbf{r},t)$ and $\rho(s)$ for a homogeneous medium under similar conditions of irradiation and detection:

$$\tilde{U}(\mathbf{r},t) = U(\mathbf{r},t) + \Delta U(\mathbf{r},t), \quad \tilde{\rho}(s) = \rho(s) + \Delta\rho(s), \qquad (3)$$

where $\Delta U(\mathbf{r},t)$ and $\Delta\rho(s)$ are the perturbations of the functions caused by inhomogeneities. The problem of optical tomography can be formulated as the reconstruction of the distributions $\mu_{\mathrm{a}}(\mathbf{r})$ and $\mu_{\mathrm{s}}(\mathbf{r})$ from the scattered radiation intensity or the probability density $\tilde{\rho}(s)$ measured at a finite number of points at the boundary of a scattering volume.

3. Pulse-modulation optical tomography

Fig. 2a illustrates the principle of probing scattering media by short light pulses, which are used in pulse-modulation tomography [31–38]. Upon detection of radiation transmitted by an object in the direction of propagation of a

probe beam, a pulse of diffusely scattered radiation is preceded by a ballistic precursor, which is caused by a non-scattered component and is delayed relative to a probe pulse by the time $\tau \approx L/c$ (where L is the thickness of a scattering medium).
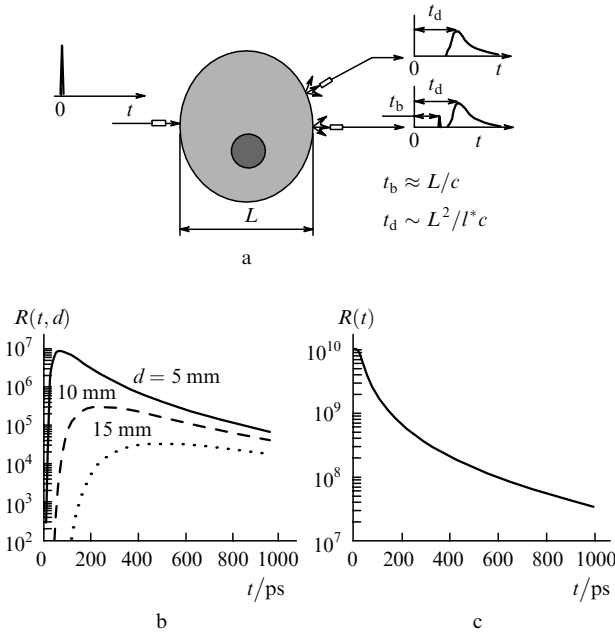
Figure 2. Pulse-modulation probing (t_b and t_d are the delay times of the ballistic and diffusion components) (a) and the shapes of pulses of diffusely scattered radiation upon probing a semi-infinite medium by a localised source and detecting radiation by a point source (b) and detecting backscattered radiation from the entire surface (c). The medium parameters: $\mu_s = 6$ cm^{-1}, $\mu_a = 0.004$ cm^{-1}, $g = 0.7$, $n = 1.4$, d is the distance between the source and detector, $R(t) = I(t)/I_0$.

The amplitude of the ballistic precursor upon probing extended objects (for example, brain) is substantially smaller than the amplitude of the diffusely scattered component. In particular, for typical values of the extinction coefficient of biological tissues $\mu_t = \mu_s + \mu_a \approx 10 - 100$ cm^{-1} within the transparency window and $L \approx 0.2$ m, the intensity of the non-scattered component will be only $10^{-90} - 10^{-900}$ of the probe-beam intensity, which imposes very strict requirements to the detection sensitivity. The shape of the pulse of a diffusely scattered component is determined by the probability density $\rho(s)$ for the specified observation conditions: $I(t - t_0) \sim \rho[c(t - t_0)]$, where t_0 is the arrival time of a probe pulse to a medium.

Figs 2b, c show the shapes of pulses of diffusely scattered radiation calculated in the diffusion approximation upon probing a semi-infinite medium by a short pulse emitted by a localised source (for example, from an optical fibre). The curves in Fig. 2b correspond to the detection of scattered radiation with a detector with a small area, which is located at different distances from the source. The curve in Fig. 2c corresponds to the detection of scattered radiation from the entire surface of the medium. The function $R(t) = I(t)/I_0$ can be interpreted as the time-dependent diffuse reflection factor of the medium. The measurements of characteristics of the diffusely scattered radiation pulse can be used for determining the optical parameters of scattering media.

The tomographic images of scattering objects can be reconstructed by detecting both the ballistic component and the diffusely scattered component. The choice of probing method imposes certain restrictions on the parameters of sources and detectors used in experiments. The ballistic component is detected by using the absorption tomography involving the formation of 'shadow' projections of the object structure. The brightness of an image in a given point is determined by the integrated absorption of the non-scattered component transmitted by the object along the chosen direction. This allows the reconstruction of images by using conventional methods of absorption tomography based on the Radon transformation.

This method imposes stringent requirements on radiation sources and photodetectors. To separate a ballistic precursor, it is necessary to use gating matched with the duration of a probe pulse. When the gate width is increased, the contribution to the detected signal from components that have experienced a few scattering events also increases, as well as the contribution from components that have experienced many scattering events but propagate predominantly along the probe beam. This reduces the contrast of the object image. The gating of the ballistic precursor should be performed with the gate width of the order of $(\mu_s c)^{-1}$, i.e., of the order of time of the light propagation between two successive scattering events. The estimate of the gate width for typical values of μ_s for biological tissues within the transparency window gives the value of the order of 1 ps. The authors of papers [39 – 41] studied the possibility of separating the ballistic and diffusion components of radiation transmitted through an object. In particular, the relation between the properties of the medium and the parameters of a probe pulse was found [40], which allows one to obtain the real bimodal shape of the detected pulse, whose first peak corresponds to the non-scattered component (see Fig. 2a).

Another circumstance, which plays an important role in tomographs based on the detection of first arrived photons, is the necessity of detecting small-amplitude pulses. This problem is solved by using photomultipliers operating in the photon counting mode and the correlation processing of successive photocounts. In the case of a considerable optical thickness of objects and biologically safe power densities of probe pulses, this requires the accumulation of many realisations of the detected signal.

The discrimination of the diffusion component for separating the ballistic precursor can be performed electronically or optically. For example, it is possible to use interference between the non-scattered component and a specially formed reference beam, in particular, in nonlinear optical media [42, 43]. The detection of a ballistic component by the method of heterodyne interferometry was considered in paper [44]. The polarisation discrimination of detected radiation [45, 46] provides an additional increase in the signal-to-noise ratio upon separation of the non-scattered component, because upon probing scattering media by linearly polarised radiation, the polarisation of the ballistic component corresponds to that of the probe radiation, whereas the diffusion component is almost completely depolarised.

Another approach to the optical gating of a ballistic precursor is the use of the light-controlled optical Kerr switches. This method was first used by the Alfano group in the USA [47 – 49]. It was shown that detection of the first

photons incident on a tissue sample *in vitro* containing an anomalous region with the high value of μ_s, which consisted of cancer cells, allows one to obtain more contrast projections of the object compared to the detection of the diffusion component. It is also possible to amplify the ballistic precursor selectively (for example, using Raman scattering [50, 51] or parametric light conversion [52].

The pulse-modulation method of probing based on the detection of the diffusion component can be also used for tomographic imaging of scattering media. This was first demonstrated in paper [53]. The requirements imposed on the time resolution and sensitivity of a pulse-modulation tomograph are not very stringent because the duration of the pulse of a diffusion component can achieve hundreds of picoseconds and its amplitude is several orders of magnitude greater than that of a ballistic precursor. The main problems encountered in this approach are related to the development of the algorithms for the reconstruction of images from the pulsed responses of the source-object-detector system measured at different points. The reconstruction procedure involves the following basic stages: (i) the subdivision of an object under study into a set of finite elements and specification of the initial values of μ_a and μ_s' for each of the elements; (ii) the choice of the optimal arrangement of sources and detectors on the object surface, which allows probing of all elements; (iii) measurements of pulsed responses for each position; (iv) calculations of pulsed responses for each position based on the specified values of μ_a and μ_s' for each element of the object; (v) comparison of the calculated and measured pulsed responses and (if necessary) correction of the initial set of values of μ_a and μ_s'.

The last two stages are repeated until the minimum of the deviation of the calculated pulsed response of the scattering medium from the measured pulsed response is found. The pulsed response can be calculated by solving numerically the nonstationary diffusion equation or using the Monte Carlo simulation. In the last decade, many efficient algorithms were developed for solving an inverse problem of the pulse-modulation optical diffusion tomography, including calculations based on the inversion Monte Carlo method.

Picosecond diode lasers emitting $\sim$ 50-ps, 10-pJ pulses in the region from 600 to 1500 nm, Q-switched solid-state lasers (in particular, a Ti:sapphire laser tunable between 690 and 980 nm), and dye lasers are used in pulse-modulation systems as radiation sources. Avalanche photodiodes, photomultipliers, and image tubes with image intensifiers (streak cameras) are used as photodetectors.

The development of modern systems of this type is based on the common principles implying the use of a multichannel system for coupling radiation to an object under study, the presence of several sources of probe radiation at different wavelengths, and the use of a multichannel system for collecting and detecting scattered radiation.

In one of such systems, radiation emitted by three diode lasers is delivered successively through an optical demultiplexer to 64 input points, which are uniformly distributed over the object surface [54]. The radiation source is connected to the corresponding input point with the help of a 1×64 switch. Scattered radiation is detected simultaneously with 64 photomultipliers operating in the photon counting mode. Photocounts are subjected to a simultaneous correlation processing in each of the 64 channels. The time of reconstruction of the object image from a set of 63×64

realisations of detected signals is approximately 30 min.

A pulse-modulation tomograph described in paper [55] also uses multichannel probing and detection. A radiation source is a Ti:sapphire laser, which provides probe pulses of a higher energy compared to diode lasers and is tunable in a broad spectral range. Laser radiation is delivered to an object through a fibre switch and 32 fibres. The scattered light is detected with a photodetector consisting of 32 fibre bundles and multianode microchannel photomultipliers. The total data accumulation time during the image reconstruction is approximately 10–20 min and is determined by the data collection time for each position of the radiation source and by the switching time of the channels of the illuminating system. Tests revealed the following problems, which are typical for pulse-modulation multichannel systems: (i) the necessity of taking into account the differences in time delays upon propagation of a probe pulse in fibres from a source to an object and from an object to photodetectors; (ii) the presence of time drifts (approximately equal to 5 ps h^{-1}) even in the case of a long warming up of the equipment; (iii) the interchannel interference of measured signals; (iv) the presence of reflections from fibre ends, which distort detected pulses.

After data accumulation, an image is reconstructed with the help of the TOAST (Temporal Optical Absorption and Scattering Tomography) program [56].

A factor that substantially restricts the real-time application of pulse-modulation optical diffusion tomography is the type of object probing – a cycle of successive switchings of a source between fibres that deliver radiation to different regions of the object. In paper [57], another method was proposed in which an illuminating system consisting of fibres of different lengths was used. The length of each of the fibres was chosen so that to provide the required delay upon propagation of pulses in adjacent fibres. Upon coupling radiation into fibres, an object is probed by a sequence of pulses, and the position of each pulse in the sequences of pulses of scattered radiation detected by photodetectors corresponds to a certain source–detector pair.

Nitrogen laser-pumped dye lasers emitting at 750 and 820 nm were used as radiation sources. The probe-pulse duration was 500 ps and the pulse repetition rate was 40 MHz. The authors note that the image reconstruction time increased when strongly scattering objects were probed because it was necessary to accumulate the realisations of detected signals.

Note that companies IDS (USA) and Philips (Holland) manufactured in 1995–1996 pulse-modulation tomographs for diagnostics of milk gland cancer [58]. An IDS tomograph uses a Q-switched Ti:sapphire laser, and the light transmitted by an object is detected with an avalanche photodiode array. Clinical tests of this tomograph revealed some technical problems caused by the instability of laser radiation and losses in optical fibres. Philips also ceased recently to manufacture its tomograph.

Nevertheless, the successful clinical applications of pulse-modulation tomographs for diagnostics of milk gland cancer and tomography of the brain of newborns were reported in Refs [58–60]. The prospects for the development of this field depend on the improvement of the equipment (the advent of reliable and low-cost short-pulse radiation sources and fast detectors, an increase in the data processing rate) and the creation of multifunctional systems for a biochemical analysis of biological tissues in real time.

4. Frequency-modulation tomography

Another method of the modulation optical tomography is based on the use of microwave-modulated probe radiation and analysis of the amplitude-phase characteristics of scattered radiation for different positions of a source and a photodetector relative to an object. Upon the diffuse propagation of modulated radiation in a scattering medium, described by equation (2), this equation in the frequency domain takes the form that is equivalent to the Helmholtz equation [9, 61]

$$\left(\nabla^2 + K^2\right) U(\mathbf{r}, \omega) = -\frac{S_0(\mathbf{r}, \omega)}{D}, \qquad (4)$$

where $K^2 = (\mathrm{i}\omega - c\mu_a)/D$. By considering the propagation of radiation with the spectrum $P(\omega)$ in an isotropic infinite medium from a point source located at the point $\mathbf{r} = 0$, we can easily obtain that, upon the harmonic modulation of the source $P(\omega) = P_{DC}\delta(\omega) + P_{AC}\delta(\omega - \omega_0)$ $(P_{DC} \geqslant P_{AC})$, the solution of equation (6) is a spherical wave, whose amplitude is described by the expression [61]

$$U_{AC}(\mathbf{r}, \omega_0) = \frac{P_{AC}}{4\pi D}$$

$$\times \exp\left\{-r\left(\frac{c\mu_a}{2D}\right)^{0.5}\left[\left(1 + \frac{\omega_0^2}{c^2\mu_a^2}\right)^{0.5} + 1\right]^{0.5}\right\}r^{-1}, \qquad (5)$$

and the wave phase is

$$\varphi(r, \omega_0) = r\left(\frac{c\mu_a}{2D}\right)^{0.5}\left[\left(1 + \frac{\omega_0^2}{c^2\mu_a^2}\right)^{0.5} - 1\right]^{0.5} + \varphi_0, \qquad (6)$$

where φ_0 is the initial phase of the wave specified by the source.

This allows us to consider transfer of harmonically modulated radiation in a medium by using the decaying photon-density waves , which are characterised by the value of the wave number equal to $[c\mu_a/(2D)]^{0.5}\{[1 + \omega_0^2 \times (c^2\mu_a^2)^{-1}]^{0.5} - 1\}^{0.5}$. The parameter $c\mu_a$ can be treated as a critical modulation frequency, which determines the decay of photon-density waves in the medium. Thus, for $\mu_a = 0.1$ cm^{-1} and the refractive index of the medium $n = 1.4$, the critical frequency is $\omega_{cr} = 2.14$ GHz. For $\omega_0 \ll \omega_{cr}$, the decay coefficient of photon-density waves weakly depends on the frequency and can be estimated as $\{3\mu_a[\mu_a + (1 - g)\mu_s]\}^{0.5}$.

It follows from the general properties of the solution of a scalar wave equation that photon-density waves should exhibit a number of the ray and wave effects, such as reflection and refraction at the interface of two media with different properties, interference of the waves from two sources, and diffraction from local inhomogeneities [62–65].

The frequency dependences of the wave number and of the decay coefficient of photon-density waves determine the relation between the resolution of the frequency-modulation method and the maximum thickness of a layer being probed, which is typical for the methods of probing scattering media with the use of wave fields. For most applications in medical diagnostics, the optimal frequency of probe radiation lies in

the range from 50 to 500 MHz. Upon probing an inhomogeneous medium with a restricted geometry, the scheme of the image reconstruction is similar to that described in this section. In this case, the amplitude and phase of the detected signal are used as characteristics measured at different positions of a source and a detector [65–72]. The possibilities of this method can be expanded, for example, by probing an object at two different wavelengths, when the phase difference of probing signals is equal to 180°.

Clinical applications of frequency-modulation optical tomography is mainly related to brain tomography (detection of endocranial hematomas, functional brain diagnostics, in particular, analysis of hemodynamics) and diagnostics of milk gland cancer (optical mammography). Fig. 3 shows the scheme of a Siemens AG optical tomograph (Germany) [73]. Four laser diodes emitting at 690 nm (the modulation frequency is 69.50 MHz), 750 nm (69.80 MHz), 788 nm (70.20 MHz), and 856 nm (70.45 MHz) are used as radiation sources. Laser radiation is delivered and scattered radiation is collected with optical fibres. Synchronous mechanical scanning of an object by transmitting and input fibres makes it possible to obtain two-dimensional projections of the inner structure of the object. The scan time required for obtaining a two-dimensional image is 2 min. Comparison of X-ray and optical tomograms of the same object shows that, in the case of a sufficiently high contrast of the latter allowing reliable diagnostics of new-growths, their spatial resolution is worse due to the diffuse propagation of light in the object. Despite this fact, optical diffusion tomography represents a promising trend in clinical diagnostics, first of all due to the use of biologically safe probe IR radiation.
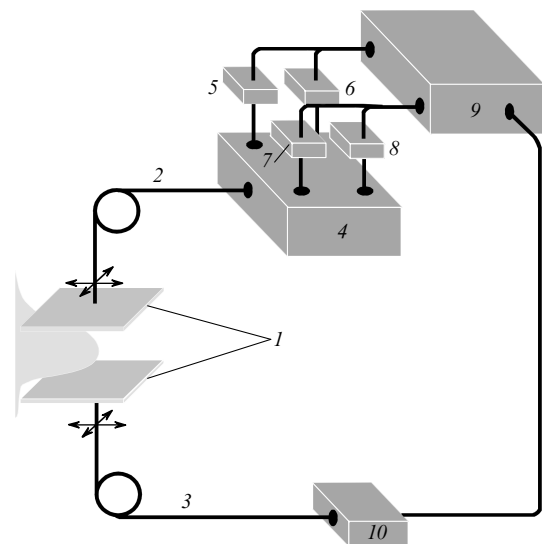

Figure 3. Scheme of a Siemens AG optical mammograph: (*1*) object positioner; (*2*) fibre delivering radiation to an object; (*3*) fibre for receiving radiation; (*4*) fibreoptic 4 × 1 multiplexer; (*5*–*8*) laser diode array; (*9*) control and processing unit; (*10*) photomultiplier.

One of the promising trends in the development of frequency-modulation tomography is related to the use of multielement phased radiation sources (method of amplitude–phase compensation) [74–76]. This approach allows one to increase the spatial resolution due to interference of

photon-density waves from different sources. When two sources are used, which emit photon-density waves of the same amplitude and frequency with the phase shift 180°, and a detector is located in the region where the path difference of the waves from the sources is zero, the amplitude of the detected signal in an isotropic scattering medium is also zero.

The presence of inhomogeneities in the region of propagation of photon-density waves results in the violation of phase matching. Experiments with model media showed that the spatial resolution in the case of localisation of an absorbing inhomogeneity achieves 1 mm; similar values are expected in the case of scattering inhomogeneities.

Fig. 4 shows the scheme of a frequency-modulation tomograph with the use of the amplitude–phase compensation [77]. The probe radiation was formed and scattered light was detected by using the principle of heterodyne processing of signals, which allows one to perform high-precision phase measurements in a low-frequency range. Eight laser diodes emitting at 780 nm were used as radiation sources. The carrier frequency was 50 MHz, and the detected frequency was 1 kHz. Radiation was detected with four photomultipliers. The laser diodes and photo-multipliers were accommodated in a housing of size 9×4 cm. The measurement cycles, corresponding to 16 different combinations of laser diodes and photomultipliers, were repeated each 16 s.
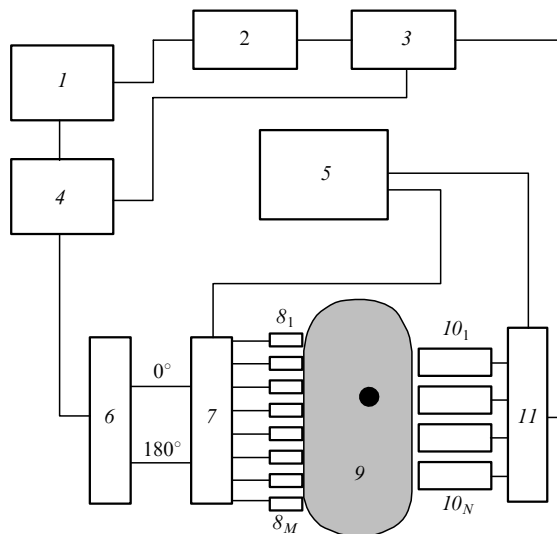
Figure 4. Scheme of an optical tomograph with phase compensation: (*1*) generator; (*2*) phase detector; (*3*) heterodyne; (*4*) modulator; (*5*) processing unit; (*6*) phase divider; (*7*, *11*) switches; ($8_1, \ldots, 8_M$) laser diodes; (*9*) object; ($10_1, \ldots, 10_N$) photomultipliers.

The use of several laser diodes emitting at different wavelengths instead of each laser diode extends the functional possibilities of the tomograph. A tomograph for functional brain diagnostics of newborns was discussed in paper [78]. In this tomograph, two lasers emitting at 750 and 830 nm were used instead of each laser diode. The use of 750-nm radiation instead of radiation at 780 nm results in a more than twofold increase in the intensity of a detected signal due to a weaker attenuation of probe radiation. A two-wavelength (750 and 830 nm) tomograph

with compensation containing nine laser diodes and 21 silicon photodiodes is described in paper [79]. This tomograph is used for diagnostics of milk gland cancer and produces high-quality images for a sampling time of about 8 s.

The authors of papers [80, 81] described a frequency-modulation tomograph for visualisation of extended scattering objects (of size up to 140 mm) with parameters that are typical for tissues within the transparency window. The probe radiation modulated at 100 MHz was produced by diode lasers emitting 15 – 30 mW at 775, 808, and 818 nm. The radiation was coupled to an object through 12 fibres of diameter 600 μm, and 32 fibres were used to collect scattered light. Scattered radiation was detected with a Hamamatsu R636-10 photomultiplier operating in the photon counting mode. The sequence of photocounts was processed by the method of time-resolved photon counting, which gave the histograms of distribution of photocounts over the modulation period. These histograms were used to obtain the amplitude – phase characteristics of the detected signal. Images were reconstructed by means of a specially developed fast projection algorithm; the reconstruction time of an object of size up to 140 mm was 5 – 10 min.

5. Optical diffusion tomography with the use of cw radiation sources

This method of diagnostics does not use modulated probe radiation, but is based on the measurement of the intensity of diffusely scattered radiation at different positions of a cw radiation source and a detector. The intensity distribution at the detection points for given positions of the source can be obtained by solving a stationary diffusion equation with the corresponding boundary conditions or by the Monte Carlo method. The visualisation of the object structure consists in the obtaining of the distribution $\mu_a(r)$ by solving the inverse problem of radiation diffusion using the intensity values measured at a finite number of points. The first attempts to obtain the images of biological objects by this method were made in 1984 – 1991 [82 – 85]. However, because the diffuse propagation of radiation hinders the reconstruction of images with the resolution and contrast that would be adequate for medical diagnostics, a further progress in optical diffusion tomography was determined mainly by the development of modulation methods.

Nevertheless, optical diffusion tomography using of continuous radiation in the wavelength range from 650 to 1200 nm is applied at present in medicine for the functional diagnostics and visualisation of the object structure. An obvious advantage of this method is its simplicity: the method does not require short laser pulses, fast photodetectors, and high-frequency devices for data processing. One of the laboratory and clinical applications of this method is the monitoring of the activity of the cerebral cortex, which does not require a high spatial resolution and is performed by the oxygenation level by measuring absorption of probe radiation at several wavelengths [86 – 89]. In [89], a tomograph is described in which a radiation sources (incandescent lamps) and detectors (photodiodes) are accommodated in a housing of size 9×4 cm. Nine sources and eight detectors combined in pairs were used. In each pair, scattered light was detected at wavelengths 760 and 850 nm through interference filters with the half-width of the transmission band equal to 9 nm.

The authors of paper [90] described a simple tomograph with a cw He – Ne laser and a CCD camera for detecting scattered radiation. In this tomograph, imaging was performed in diffusely scattered light. The tomograph allowed the visualisation of inhomogeneities in a strongly scattering medium at the depth up to 1.5 cm. A fast algorithm for the reconstruction of quasi-three-dimensional images of optical inhomogeneities was developed.

6. Algorithm for solving inverse optical diffusion tomography problems

At present, many algorithms for solving inverse optical diffusion tomography problems have been developed [91 – 103]. A detailed description of these algorithms is beyond the scope of this review. We will consider here the principles of solving inverse problems, which can be used in different optical diffusion tomography modifications, for some examples characterised by original approaches. In particular, the authors of paper [96] proposed the method for reconstructing images in frequency-modulation tomography from a set of the measured values of the amplitude and phase of scattered radiation. The algorithm is based on the methods of the perturbation theory, according to which the spatial distributions of μ_a and μ_s' in the volume being probed can be represented in the form

$$\mu_a(\boldsymbol{r}) \Rightarrow \mu_a^0 + \Delta\mu_a(\boldsymbol{r}); \quad \mu_s'(\boldsymbol{r}) \Rightarrow \mu_a'^0 + \Delta\mu_s(\boldsymbol{r}). \tag{7}$$

The Helmholtz equation should be replaced by the equation for the perturbed values of the intensity of the diffusion component

$$\left[\nabla^2 + K^2\right]U(\boldsymbol{r}) = \frac{\delta(\boldsymbol{r})}{D_0} + \lambda\Lambda(\boldsymbol{r})U(\boldsymbol{r}), \tag{8}$$

where λ is a parameter; K and D_0 correspond to the unperturbed parameters of the object; the function $\Lambda(\boldsymbol{r})$ is determined by the perturbations of μ_a and μ_s'. The complex amplitude of a photon-density wave can be expanded into a series in powers of λ

$$U_{AC}(\boldsymbol{r}) = U_{AC0}(\boldsymbol{r}) + \lambda U_{AC1}(\boldsymbol{r}) + \lambda^2 U_{AC2}(\boldsymbol{r}) + \ldots, \tag{9}$$

where a term of the order N is determined by the recurrent expression

$$U_{ACN}(\boldsymbol{r}_d) = \int G(\boldsymbol{r}, \boldsymbol{r}_d)\Lambda(\boldsymbol{r})U_{ACN-1}(\boldsymbol{r})d^3\boldsymbol{r}; \tag{10}$$

$\boldsymbol{r}_d$ determines the position of a detector; and $G(\boldsymbol{r}, \boldsymbol{r}_d)$ is the Green function for the Helmholtz equation.

The coefficient μ_s' can be considered constant over the volume for many applications, and fluctuations of μ_a can be assumed small and gradually changing. In this case, $\Lambda(\boldsymbol{r}) \approx c\Delta\mu_a(\boldsymbol{r})/D_0$, and only the linear term in expansion (9) can be considered in calculating the amplitude and phase of the photon-density wave. By dividing the volume being probed into n elements of size h, we can reduce the problem of reconstruction of $\mu_a(\boldsymbol{r})$ to the solution of a system of linear equations

$$\begin{pmatrix} U_1(\boldsymbol{r}_s, \boldsymbol{r}_d)_1 \\ U_1(\boldsymbol{r}_s, \boldsymbol{r}_d)_2 \\ \cdots\cdots\cdots \\ U_1(\boldsymbol{r}_s, \boldsymbol{r}_d)_m \end{pmatrix} = \begin{pmatrix} T_{11} \ldots T_{1n} \\ T_{21} \ldots T_{2n} \\ \cdots\cdots\cdots \\ T_{m1} \ldots T_{mn} \end{pmatrix} \begin{pmatrix} \Delta\mu_a(\boldsymbol{r}_1) \\ \Delta\mu_a(\boldsymbol{r}_2) \\ \cdots\cdots \\ \Delta\mu_a(\boldsymbol{r}_n) \end{pmatrix}, \tag{11}$$

where the matrix elements T_{km} can be represented in the form

$$T_{km} = G(\boldsymbol{r}_{dk}, \boldsymbol{r}_m)U_0(\boldsymbol{r}_{sk} - \boldsymbol{r}_m)\frac{h^3}{cD_0}.$$

The authors of papers [97 – 100] considered the efficient algorithms for solving inverse optical diffusion tomography problems using the method of 'average trajectories'. The method is based on the fundamental property of the solution of the diffusion equation, which is manifested in the relation between the functions $U(\boldsymbol{r}, t)$ and $U(\boldsymbol{r}_l, \tau)$ in the form of the integral transformation with the Green function of the diffusion equation as a kernel. This relation allows one to represent the relative change $\Delta I/I$ in the optical signal caused by inhomogeneities of the object in the form of a curvilinear integral over the trajectory describing the position of the centre of a photon cloud propagating in the medium from a source to a detector:

$$-\ln\left(1 - \frac{\Delta I}{I}\right) = \frac{c}{n}\int_0^{L_{ph}} \frac{\langle\delta\mu_a\rangle(l)}{(l)}\,dl, \tag{12}$$

where L_{ph} is the mean photon path in the medium; $v(l)$ is the instant rate of propagation of the photon cloud along the trajectory; and $\langle\delta\mu_a\rangle(l)$ is the change in the absorption coefficient along the trajectory. Here, we can see the analogy between diffusion tomography and absorption tomography, when the signal attenuation is caused by absorbing inclusions along the probe-beam trajectory.

Nonlinear statistical algorithms for solving inverse optical diffusion tomography problems in real time were described in papers [80, 81, 101, 102]. The algorithms are based on the hypothesis about the interrelation between the probability P_{ij}' of detecting an inhomogeneity in the ijth measurement and from the difference between photon fluxes detected in the presence or the absence of an inhomogeneity in the object: $P_{ij}' \sim \Phi_{ij}' - \Phi_{ij}$. The spatial distribution P_{ij}' is determined by the probability density $p_{ij}'(\boldsymbol{r}) \sim P_{ij}'f_{ij}'(\boldsymbol{r})$, where $f_{ij}'(\boldsymbol{r})$ is the three-dimensional distribution of the probability of propagation of photons through the point with the coordinate $\boldsymbol{r}$ of the object detected in the ijth measurement.

The reconstruction of the image of the object structure consists in the determination of a complete three-dimensional distribution of the probability of finding inhomogeneities at different points of the object, which is defined by the product $\prod_{ij} P_{ij}'f_{ij}'(\boldsymbol{r})$. The values of $\Delta\Phi_{ij} = \Phi_{ij}' - \Phi_{ij}$ required for this are obtained from the experiment, while the values of $f_{ij}'(\boldsymbol{r})$ are determined from Monte Carlo simulations or by using approximate analytic methods. Experiments with model objects containing absorbing inhomogeneities have demonstrated a fast operation of the algorithm along with an adequate quality of reconstructed images.

7. Optical coherent tomography

The method for studying tissue structures, which is called optical coherent tomography and is based on the low-coherence interferometry, was first proposed in papers [104, 105]. At present, several hundreds of papers devoted to the application of optical coherent tomography for a morphological analysis and visualisation of tissue structures have been published. We will mention here only the most important papers. These are the studies of the groups at the Vienna University (Austria) [104–107], Massachusetts Institute of Technology (USA) [108–110], and at the Institute of Applied Physics, RAS (Nizhnii Novgorod, Russia) [111–115].

Fig. 5 shows the scheme of a fibre interferometer with a low-coherence source applied for the visualisation of the object structure. Scanning of the object over the depth (in the z direction) is performed by moving a reflector in a reference arm of the interferometer. In this case, the amplitude of the detected signal is proportional to the local value of the reflection coefficient of the medium at the probing depth. Scanning in the transverse direction is performed by moving the probe-beam axis with the help, for example, an electromechanical scanning system.
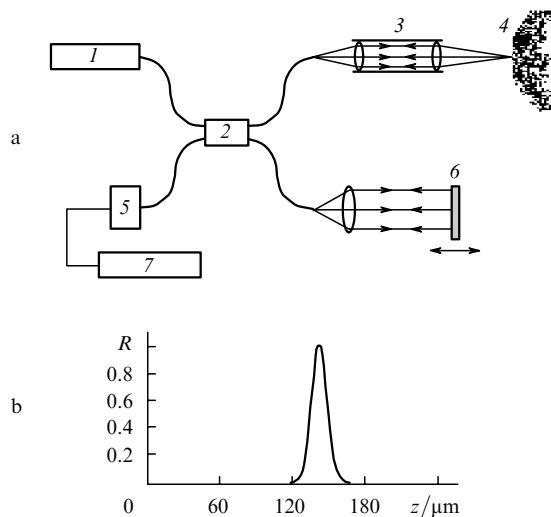

Figure 5. (a) Scheme of a fibreoptic interferometer with a partially coherent radiation source used in optical coherent tomography: (*1*) source; (*2*) fibreoptic interferometer; (*3*) object channel; (*4*) object; (*5*) detector; (*6*) reference channel; (*7*) processing unit. (b) Typical pulsed response of the optical coherent tomography system.

The presence of local regions in the medium under study with optical characteristics that differ from the average values leads to a change in the amplitude of the detected signal. Therefore, the time dependence of the signal amplitude during one cycle of longitudinal scanning can be used for the reconstruction of the distribution of the reflection coefficient over the depth for a specified position of the probe beam.

In practice, the signal-to-noise ratio is increased by averaging the local values of the reflection coefficient, which were obtained from the sequence of realisations of the detected signal upon periodic scanning the given region of a sample. Fig. 6 shows the shape of the output signal of the

optical coherent tomography system obtained for model media (gel base with polystyrene microparticles as a filler). The peaks of the detected signal at the initial and final stages of the longitudinal scan cycle are caused by reflections from the walls of a cell with a sample. The attenuation of the signal with depth is determined by the distribution of μ_t.
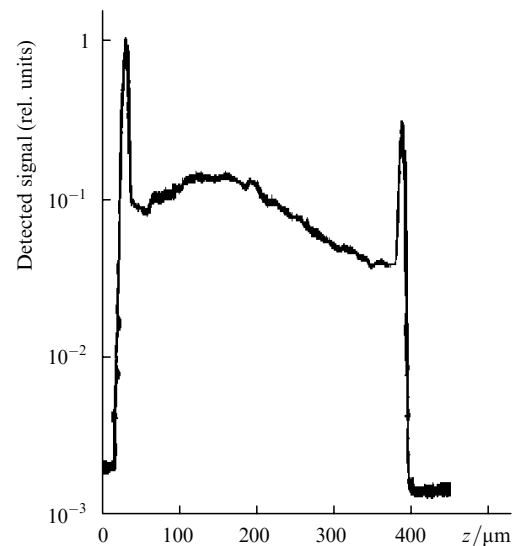
Figure 6. Shape of the output signal of a low-coherence interferometer upon probing a model object.

The maximum probing depth of scattering media is small and comparable with the transport depth l^*, i.e., it is of the order of millimetre. For this reason, optical coherent tomography is now applied in medicine mainly for optical biopsy of the surface layers of tissues *in vivo*. A specific field is a visualisation of the inner structure of the human eye. The eye tissues, except sclera and retina, have small extinction coefficients, so that a high signal-to-noise ration can be achieved upon probing over the entire depth. Papers [104–107, 109, 116–121] are devoted to various applications of optical coherent tomography in ophthalmology.

An important parameter of an optical coherent tomograph is its resolution over depth, which depends on the width of the source spectrum and is described by the expression

$$\Delta z = \frac{2 \ln 2}{\pi} \frac{\lambda_c^2}{\Delta \lambda}, \tag{13}$$

where λ_c is the central wavelength and $\Delta \lambda$ is the half-width of the emission spectrum. Therefore, if a superluminescent diode with $\lambda_c = 820$ nm and $\Delta \lambda = 20$ nm is used as a radiation source, then Δz will be approximately 15 μm. The resolution of optical coherent tomography systems can be improved by using broadband radiation sources and detectors. As radiation sources, either cw laser diodes (superluminescent diodes or lasers operating below the threshold) or repetitively pulsed lasers emitting ultrashort pulses are used. In the latter case, it is necessary to use picosecond and subpicosecond probe pulses to obtain a sufficient resolution over depth.

The development of an optical coherent tomography system with a micron resolution was reported in paper [122].

A radiation source was a Q-switched Ti:sapphire laser with $\Delta\lambda \sim 350$ nm and $\lambda_c = 800$ nm, which gives the resolution $\Delta z \sim 1$ µm. Such a broad laser emission band was achieved due to the use of specially manufactured cavity mirrors and intracavity dispersion compensators. The design of a fibre interferometer was optimised (Fig. 7) to reduce the dispersion distortions of an optical signal. This was achieved by using fibre polarisation elements and compensators of phase distortions. The half-width of the pulsed response function of this system was 1.5 µm, which provides the visualisation of the tissue structure with the intracell resolution. In particular, the tomographic images of cellular structures of a tadpole of the African frog are presented in [122]. They were obtained with a resolution of 1×3 µm and allow one to identify different organelles inside cells and to analyse the dynamics of the development of the cellular structure (different stages of mitosis for several cells are shown). However, paper [122] only demonstrates the possibilities of the method, because the complexity of such systems and a high cost of radiation sources and optical elements of the interferometer restrict their use in clinics.
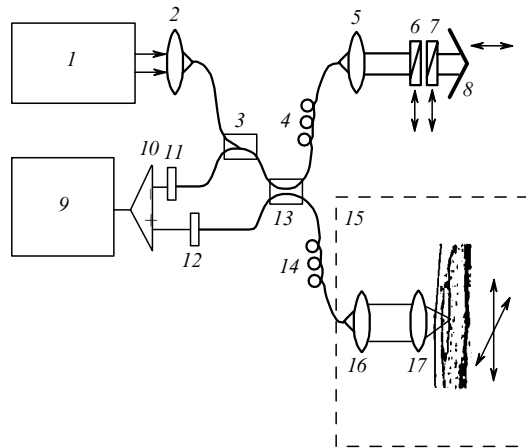

Figure 7. High-resolution femtosecond laser optical coherent tomography system: (*1*) Ti:sapphire laser; (*2, 5, 16, 17*) lenses with compensation for dispersion distortions; (*3, 13*) fibreoptic couplers; (*4, 14*) fibreoptic polarisers; (*6, 7*) dispersion – distortion compensators; (*8*) reference mirror; (*9*) processing unit; (*10*) amplifier; (*11, 12*) detectors; (*15*) system for transverse scanning of a sample.

The use of additional devices, in particular, fibreoptic endoscopes and catheters extends the field of clinical applications of optical coherent tomography. Fibreoptic endoscopes and catheters developed for the optical coherent tomography diagnostics, including endarterial endoscopy, are described in papers [123 – 125]. In the case of endarterial probing [123, 124], the transverse scan of a part of the vessel surface is performed by the axial rotation of the light-guiding single-mode fibre-microprism system with the help of a step motor via a reduction gear. Various fibreoptic tools for optical coherent tomography systems are described in paper [125]. The transverse scan of a region under study is performed with a piezoelectric microscanner by moving the output end of a single-mode fibre in the object plane of a single-lens or two-lens optical system. In this case, the size of the scanned region is determined by the transverse magnifi-

cation of the lens system used and can be varied depending on the problem to be solved.

A variety of diagnostic possibilities of optical coherent tomography systems in stomatology, urology, otolaryngology, and gastroenterology were demonstrated in paper [126]. The optical coherent tomography monitoring of processes of laser interaction with tissues (laser modification and ablation) was described in papers [127 – 129]. The real time optical coherent tomography control of laser ablation of tissues was demonstrated in paper [130]. Fig. 8 shows the scheme of the setup for laser ablation of tissues with the optical coherent tomography system used for feedback. The local ablation is performed with a $1 – 3$ W argon laser. Laser radiation is delivered to a sample through a fibre and is focused to a spot of diameter 0.8 mm on the sample surface. A superluminescent diode emitting at 1.3 µm is used as a radiation source in the optical coherent tomography system. The width of its emission spectrum corresponds to a longitudinal resolution of 18 µm (in a free space) and the signal-to-noise ratio is 115 dB for the diode power of 5 mW. Ablation experiments were performed with a muscular tissue of rats, which was exposed for 10 s to 3-W laser radiation. After irradiation, a sample was displaced with the help of a scanner to obtain a three-dimensional image of the ablation crater. The image of the ablation region was reconstructed by using 60 sections obtained at 100-µm intervals. The sequential images of the region allow the identification of different stages of laser interaction with the tissue, till the tissue charring inside the ablation crater.
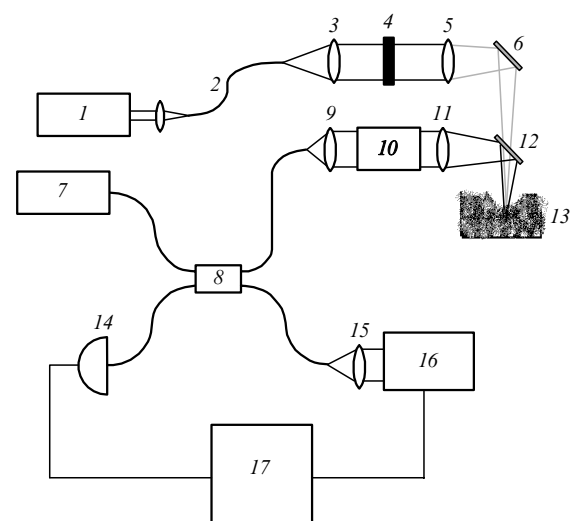
Figure 8. System for laser ablation of tissues with optical coherent tomography monitoring: (*1*) argon laser; (*2*) fibre for delivering radiation from an argon laser; (*3, 5, 9, 11, 15*) collimating lenses; (*4*) beam chopper; (*6*) mirror; (*7*) superluminescent diode; (*8*) fibreoptic interferometer; (*10*) two-coordinate scanner; (*12*) dichroic mirror; (*13*) sample; (*14*) detector; (*16*) optical delay line; (*17*) processing unit.

8. Various modifications of the optical coherent tomography method

The successful applications of optical coherent tomography for morphological analysis of tissues stimulated the further development of this method, resulting in the appearance of

some modifications of optical coherent tomography with additional functional possibilities.

(1) Multiwave, or spectrally sensitive optical coherent tomography. The potential possibilities of low-coherence interferometry with two radiation sources (830 and 1285 nm) for a noninvasive morphological analysis and visualisation of tissue structures *in vivo* were considered in paper [131]. Two fibreoptic Michelson interferometers were used, with a common reflector in reference channels. The probe beams were made coincident with the help of a dichroic mirror. A two-wavelength scheme was used in [132] for analysis of the concentration of water in model intralipid media. The possibility of analysis of optical coherent tomography images in the spectral range from 650 to 1000 nm using a femtosecond Ti:sapphire laser was considered in paper [133].

The detection method based on the spectral selection of radiation in the optical coherent tomography system was described in paper [134]. The detection system consists of a beam-expanding telescope, a diffraction grating, and a CCD camera. The CCD camera detects the wavelength-dependent intensity of the interference pattern produced due to a superposition of the object and reference beams. The window Fourier transform of the interference patterns was used for analysis of the absorption spectra of objects at different depths. Thus, the spectrally sensitive low-coherence probing of tissues expands the functional possibilities of the conventional optical coherent tomography method.

(2) Polarisation-sensitive optical coherent tomography. This method also provides additional possibilities compared to the conventional optical coherent tomography. It was shown in paper [135] that the polarisation selection of detected radiation in a low-coherence interferometer during the formation of an interference signal with the use of a co-polarised or a cross-polarised component can be applied for the size discrimination of scattering centres in a region being probed during imaging. This is possible because the degree of residual polarisation of radiation scattered by large and small particles is different.

Another, polarisation-sensitive optical coherent tomography method for studying structural variations in the skin caused by burning was proposed in paper [136]. The method is based on the analysis of variations in the birefringence of the skin collagen caused by its thermal denaturation. The polarisation of the source radiation at 1310 nm with the half-width of the emission spectrum equal to 75 nm was modulated. By detecting the interference signals for orthogonally polarised components of the detected radiation at different polarisation states of the incident beam, the authors [136] determined the Stokes parameters of the scattered light, thereby measuring the optical anisotropy of the tissue as a function of the penetration depth. The tissue structure was visualised by reconstructing the distributions of the phase difference of two orthogonally polarised components of scattered radiation. The slope of the dependence of the phase difference on the penetration depth yields the thickness of the burnt skin layer.

A similar method of low-coherence *in vitro* diagnostics of various tissues (human tooth enamel and dentine, pig and chicken cardiac muscles, etc.) based on the measurements of optical anisotropy at different depths was considered in papers [137, 138]. The schemes of the optical coherent tomography systems used in these papers differ in the

method of analysis of the polarisation state of scattered radiation from that applied in [136]. They use circularly polarised probe radiation and the detection of two orthogonally polarised components of radiation scattered by an object. In addition, unlike a conventional optical coherent tomography system, not only the signal envelope is analysed but also the amplitude–phase characteristics for both detection channels. The application of polarisation-sensitive optical coherent tomography for diagnostics of burns by measuring the optical anisotropy of a thermally denaturated collagen as a function of depth was described in paper [139].

(3) Doppler optical coherent tomography. By combining optical coherent tomography with Doppler diagnostics, it is possible to develop multifunctional systems for visualisation of morphological properties of tissues and the hemodynamics at different depths in tissues. This method was first applied in paper [140], where the velocity of liquid flows was measured in model media with the 5-μm resolution and the measurement error 7%. The physical foundations of probing of nonstationary scattering media, in which the dynamics of scattering centres substantially depends on the depth, by using partially coherent radiation, were discussed in paper [141].

The authors of [141] studied aqueous suspensions of polystyrene spheres with different diameters in a two-section cell, which was divided by a glass plate. The probing at different depths was performed by adjusting a low-coherence interferometer, and the dynamics of scattering centres was studied using the spectral analysis of fluctuations of the detected interference signal (without scanning over the depth).
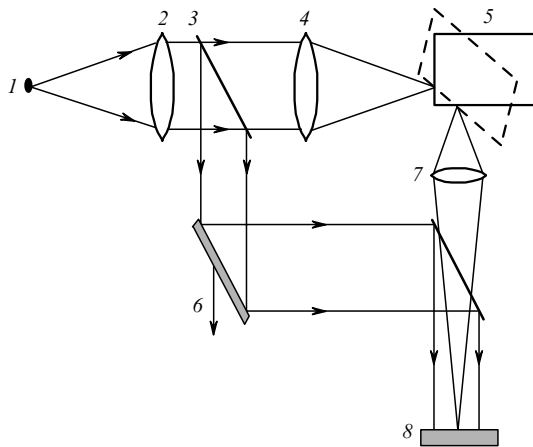
The low-coherence Doppler tomography of tissues with the use of picosecond probe laser pulses was performed in paper [142]. The setup consisted of a Michelson interferometer and a photomultiplier, whose output signal was fed, after low-frequency filtering and amplification, to a spectrum analyser. The radiation sources were a laser diode (the emission wavelength $\lambda_c = 675$ nm, the pulse duration $\tau_p = 300$ ns, the pulse repetition rate $f_p = 700$ kHz, and the output power $P = 0.5$ mW), a frequency doubled, Q-switched neodymium laser ($\lambda_c = 527$ nm, $\tau_p = 35$ ps, $f_p = 76$ MHz, $P = 1 - 3$ mW), and a dye laser pumped by the neodymium laser ($\lambda_c = 578$ nm, $\tau_p = 5 - 8$ ps, $f_p = 3.8$ MHz, $P = 205$ mW). The measurements of the velocity of the scattering medium with accuracy sufficient for analysis of the hemodynamics in tissues were demonstrated for all radiation sources. The selection of a Doppler signal over the depth can be performed by scanning a reflector in the reference channel.

A group at the Beckman Laser Institute (University of California, USA) [143–148] and a group [149] have recently made substantial contributions to the development of this field. Among the original approaches in the development of new methods of Doppler optical coherent tomography are the creation of a phase-sensitive Doppler optical coherent tomography system [146] and a further development of this approach with the use of an optical Hilbert processor based on the interference of polarised light beams [147].
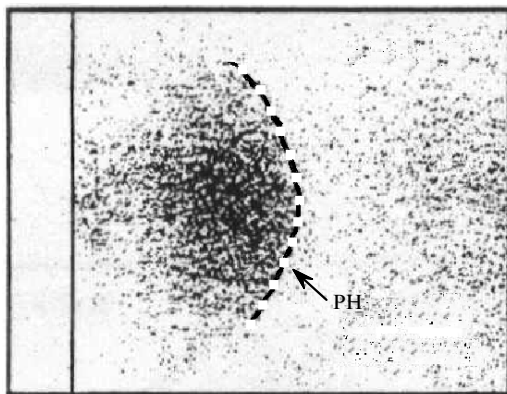
(4) The authors of papers [150, 151] proposed an ingenious modification of the optical coherent tomography method, which they called the 'photon horizon technique'. The principle of this technique is illustrated in Fig. 9. An object under study is used as a diffusion reflector in one of the arms of a Mach–Zehnder interferometer. The intensity

distribution obtained due to the superposition of scattered radiation and a reference beam is detected with a CCD camera. When the path difference between scattered radiation and the reference beam is smaller than the coherence length of the source, the speckle-modulation of the detected image will be observed; otherwise the stochastic interference modulation of the image is suppressed. By changing the length of the reference arm, one can separate the components of scattered light with a specified propagation time in the medium. To exclude the background incoherent component, two images are successively recorded at the two lengths of the reference arm differing by $\lambda/2$ (the mirror in the reference arm is mounted on a piezoceramic translator). Due to the subtraction of the images, the region of speckle-modulation, corresponding to the specified time of radiation propagation in the object, is localised (Fig. 10). The application of this method for the visualisation of inhomogeneities in tissues (human skin) shows that it can be used for diagnostics of skin tumors (in particular, melanoma).

(5) Optical tomography by analysing the speckle contrast upon partially coherent illumination. This method, which was proposed in paper [152], also can be considered as a specific variant of optical coherent tomography. In this method, the measurement of the contrast of speckle fields upon multiple scattering of probe quasi-monochromatic radiation as a function of the conditions of the object illumination and detection of scattered light is used for visualisation of inhomogeneities.

The influence of the width of the emission spectrum of a source on the contrast of speckles observed in scattered light is caused by the suppression of interference of the components of scattered light under the condition that the path difference for these components exceeds the coherence length of radiation. Because the distribution of the paths of the components depends on the distributions of parameters of the scattering medium (μ_a and μ_s'), the measurements of speckle contrasts at different positions of the source and detector can be used for the reconstruction of the object image.

(6) Frequency-sweep optical tomography. This method [153] differs from conventional optical coherent tomography by the use of probe radiation with the coherence length exceeding the maximum path difference between the interfering reference and object beams. The selection over the depth is performed by tuning linearly the probe frequency during the scan cycle. The autocorrelation function of the distribution of the reflection coefficient over the depth is obtained from the inverse Fourier transform of the dependence of the output signal of a detector on the instantaneous frequency of probe radiation. The frequency sweep is performed using a tunable laser diode (tuned near 852 nm within 0.8 nm) or a semiconductor laser with a diffraction grating employed as an external cavity mirror (tunable from 771 to 791 nm). Experiments with model media have demonstrated the possibility to analyse the dependence of optical characteristics (in particular, g) on the depth, the maximum probe depth being approximately $2.4l^*$. The additional possibilities for analysis of tissues (for example, bloodstream parameters) can be realised by forming a train of probe pulses with alternating shapes of frequency dependences (each even pulse has a constant frequency for measuring Doppler shifts, while each odd pulse has a linearly changing frequency for the structure visualisation).

Figure 9. Scheme of a low-coherence interferometer [150, 151]: (*1*) partially coherent source (laser diode operating below the threshold); (*2*) collimating lens; (*3*) beamsplitter; (*4*) focusing lens; (*5*) object; (*6*) movable cavity mirror; (*7*) objective; (*8*) CCD array.

9. Speckle-correlation optical tomography

When coherent radiation is scattered in nonstationary media, the dynamic speckle-modulation of scattered light takes place. In this case, the correlation characteristics of intensity fluctuations depend on the dynamic and optical parameters of a medium and the scattering geometry. The intensity fluctuations are caused by the stochastic interference of the components of the scattered field with random frequency shifts accumulated due to successive events of scattering by moving scatterers. If the parameters of the medium are known for a given scattering geometry, the dynamic characteristics of a scattering system can be determined by measuring the correlation time of the intensity fluctuations.

This method for studying scattering nonstationary media, which is called diffusing-wave spectroscopy (DWS), was proposed in papers [7, 154]. The models, which are used to describe the quasi-elastic scattering of light, give the relation between the dynamic characteristics of a scattering system with the correlation function $G_1(\tau) =$


Figure 10. Localisation of the probed zone by the speckle-modulation region on the object image (PH: photon horizon).

$\langle E(t)E^*(t+\tau)\rangle$ of fluctuations of the scattered field, whereas in experiments the correlation function $G_2(\tau) = \langle I(t)I(t+\tau)\rangle$ of intensity fluctuations is usually measured. The relation between the normalised correlation functions $g_1(\tau) = G_1(\tau)/G_1(0)$ and $g_2(\tau) = G_2(\tau)/G_2(0)$ is described by the Sigert formula [155] $g_2(\tau) = 1 + \beta|g_1(\tau)|^2$ (the coefficient β is determined by the detection conditions), which is valid for many scattering media.

Analysis of the correlation characteristics of a signal at different positions of a source and a detector upon probing a scattering medium with dynamic inhomogeneities (regions where the mobility of scatterers differs from the average mobility) can be used for the reconstruction of the object image using the diffusion model of correlation transfer in a dynamic scattering medium [156]. According to this model, the space–time evolution of the correlation function $G_1(r, \tau)$ in a nonstationary optically thick medium is described by the diffusion equation

$$\left[D\nabla^2 - c\mu_a - \gamma^2(\tau)\right]G_1(r, \tau) = -cS(r), \qquad (14)$$

where the term $\gamma^2(\tau)$, determined by the dynamic properties of the medium, describes the additional effect of 'absorption' of the correlation in the nonstationary medium. When a standard cw coherent radiation source is used, the problem of reconstruction of the distribution of dynamic characteristics described by the parameter $\gamma^2(r, \tau)$ is reduced to the solution of a standard optical coherent tomography problem.

This method was used in [157] to obtain the tomograms of a scattering object with dynamic inhomogeneities. A model object was a cylinder made of a polymer with titanium dioxide filler. A spherical cavity inside the cylinder was filled with an aqueous solution of intralipid (Fig. 11). The optical parameters μ_s' and μ_a of the cylinder and solution were chosen so that to exclude the possibility of visualisation of the cavity by the methods of modulation optical tomography. The diffusion coefficient of scatterers in a nonstationary medium was 1.5×10^{-8} cm^2 s^{-1}. Laser radiation was coupled to the object through a fibre. Scattered radiation was detected at points uniformly distributed (in $30°$ intervals) over the sample surface. Radiation was detected with a photomultiplier operating in the photon counting mode. The image of a dynamic inhomogeneity was reconstructed using the calculated values of the diffusion coefficient as the visualisation parameter (Fig. 11).
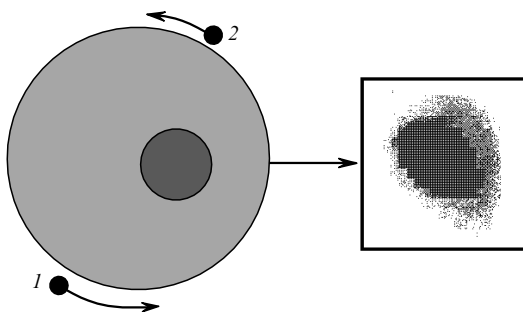
Figure 11. Tomogram of a dynamic inhomogeneity in a model object: (*1*) coherent radiation source; (*2*) detector; the arrows show the direction of the object scan.

Applications of correlation tomography for diagnostics in medicine concerned first of all the study of the hemodynamics in tissues at probe depth of the order of $1-2$ mm. In particular, the diagnostics of burns was performed for measuring the thickness of a necrotic layer [158]. The principle of this diagnostics is illustrated in Fig. 12. Clinical experiments with animals have demonstrated the efficiency of this method for probing skin burns at the depth up to 1.5 mm. The average value of the slope of the correlation function in a specified interval τ was used as a diagnostic parameter.
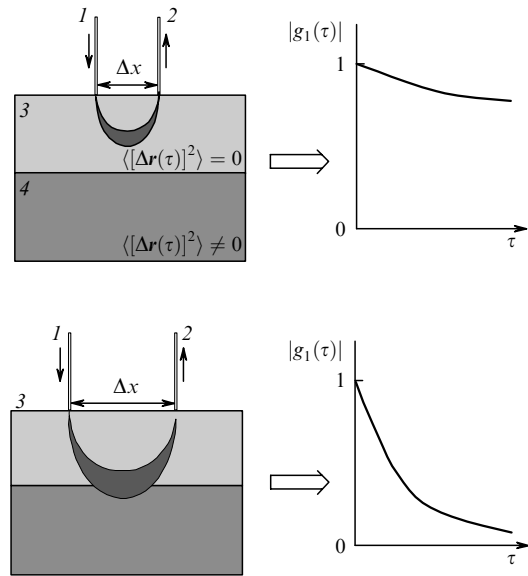
Figure 12. Principle of the speckle-correlation probing of burnt tissues: (*1*) fibre delivering coherent probe radiation; (*2*) fibre delivering scattered radiation to a detector; (*3*) burnt necrotic tissue layer [scattering centres (red blood cells) are immobile; $\langle[\Delta r(\tau)]^2\rangle = 0$ is the dispersion of displacements of scattering centres for the time τ; (*4*) deep layer of a healthy tissue with moving red blood cells ($\langle[\Delta r(\tau)]^2\rangle \neq 0$). An increase in the probe depth with increasing the distance Δx between a source and a detector results in the penetration of probe radiation to a healthy tissue layer and in faster decay of the autocorrelation function of the scattered-field amplitude fluctuations with increasing τ.

A variant of the speckle-correlation functional diagnostics of tissues containing dynamic scatterers (for example, red blood cells in a microcirculatory vessel) is a simple method based on local estimates of the contrast of time-averaged speckle-modulated object images. This method was proposed in papers [159–162] (Fig. 13) and is called LASCA (laser speckle contrast analysis). It is based on the use of the ergodicity hypothesis to the limited regions of dynamic speckle fields for which the spatial distributions of instantaneous intensities are statistically homogeneous. The estimates of the static moments of intensity fluctuations, obtained after processing of time realisations of the detected signal at a fixed point, are equivalent to the estimates over the spatial realisations of the intensity values (under the condition of local stationary fluctuations during analysis). This gives the relation between the contrast $V(T) = \sigma_1(T)/\langle I\rangle$ of the dynamic speckle pattern, detected with a specified exposure time T [$\sigma_1(T)$ is the exposure-time-dependent root-mean-square fluctuations of the brightness

of a speckle-modulated image; and $\langle I \rangle$ is the average brightness of the image], and the decorrelation time [162], which is determined by the average value of scattering centres at a distance of the order of the radiation wavelength.
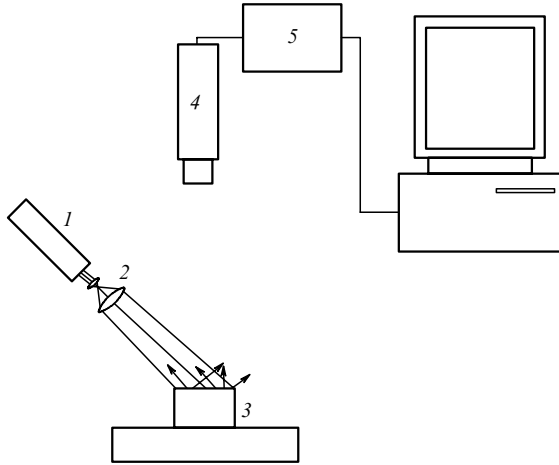
Figure 13. Visualisation of nonstationary scattering media using local estimates of the contrast of time-averaged speckle-modulation images: (*1*) laser; (*2*) telescopic system (beam expander); (*3*) object; (*4*) CCD camera; (*5*) PC video-signal interface board.

In a number of papers devoted to the study of the dynamics of red blood cells in microcirculatory vessels by this method, a model of dynamic scattering with the Lorentzian spectrum of intensity fluctuations and the corresponding exponential function $g_2(\tau)$ was used. This model correctly describes qualitatively the decay of the correlation function. The exposure time T_d, which corresponds to a specified decrease in the contrast of the time-averaged speckle-modulated image, and the velocity $\langle v \rangle$ of red blood cells averaged over a layer being probed are related by a simple expression $T_d = K\lambda/\langle v \rangle$, where K is the normalisation coefficient. The exposure time T_d is found by recording the sequence of images of the object surface during different times T. An important problem is the measurement of the absolute values of $\langle v \rangle$, for which the coefficient K should be known, which depends on the optical characteristics of tissue in a complicated way. The calibration of the system with the help of models is not always adequate for real objects. The errors in the measurement of $\langle v \rangle$ by this method can be caused by the following reasons [163]:

(i) depolarisation of scattered radiation, which reduces the contrast;

(ii) the nonzero contrast for the values of T substantially exceeding the decorrelation time, which is caused by the presence of immobile scatterers in the probed volume along with mobile scatterers (resulting in a substantial residual contrast);

(iii) the instrumental components of the systematic error caused by the dark noise and the CCD camera noise and the nonlinearity of its transfer characteristics, etc.

For this reason, in these systems for diagnostics of the hemodynamics in surface layers of tissues, as a rule, the relative variations in the velocity $\langle v \rangle$ are analysed. The method allows the functional visualisation of the analysed region by reconstructing two-dimensional distributions of the local estimates of $V(T)$ for T being fixed. The size of a spatial window for the local estimates of $V(T)$ should exceed considerably the average size of speckles in the image plane. An important condition, which determines the image quality, is the choice of the optimal size of speckles, which will provide the minimal distortions of the statistics of intensity fluctuations for the specified spatial resolution, sensitivity, and dynamic range of the CCD camera. By using the colour or brightness image coding, the two-dimensional distributions of the level of blood microcirculation in the surface layers of tissues can be obtained. Applications of LASCA for the functional diagnostics and visualisation of various tissues and organs were reported in a number of papers. From the point of view of the clinical applications of monitoring systems in cerebral surgery, it is interesting to compare this method with other methods used for monitoring the hemodynamics in the brain cortex of rats [164]. The diagnostics of burns with the help of a modified LASCA with the use of a focused laser beam was discussed in paper [165].

10. Optoacoustic tomography

Optothermal or optoacoustic response of a tissue to pulsed laser irradiation underlies optoacoustic tomography, which combines the advantages of optical, thermal, and acoustic probing of tissues [166–168]. Pulsed heating of a tissue changes its own thermal radiation, and this effect is used in pulsed optothermal radiometry. The maximum of thermal radiation of living objects lies at 10 μm. The optothermal radiometry signal is determined by the temperature distribution in an object, the heat conductivity of a medium, and the absorption coefficients at the probe wavelength (μ_a) and the thermal radiation wavelength (μ_a') (10 μm). The spatial distribution of μ_a is determined from the measured optothermal radiometry signal [169].

The thermal response time τ_T of an object of size h is approximately equal to h^2/a_T. The typical value of the thermal diffusivity for many tissues is $a_T \approx 1.2 \times 10^{-7}$ m^2 s^{-1} [166, 167]. Therefore, the thermal relaxation time, which is determined by the object size, is, for example, 10^{-3} s for a cell, and is approximately 3×10^{-2} s for a small artery. Irradiation of a tissue by short light pulses (much shorter than τ_T) produces a temperature distribution in it, which reflects the tissue structure.

The detection of the surface temperature (the optothermal radiometry signal) in time allows one to find the temperature distribution inside the tissue, thereby visualising hidden inhomogeneities caused by local variations in the absorption coefficient at the wavelength of probe radiation [169]. The main disadvantage of this method is that it is quite difficult to find the temperature distribution over the depth.

On the other hand, the pulsed optoacoustic method yields reliable results in the case of strong scattering of light [167, 168, 170]. The method is based on the thermal mechanism of generation of acoustic vibrations in a medium upon absorption of laser pulses and the detection of the time profile of induced pressure waves. The optoacoustic signal is proportional to the absorption coefficient and the local intensity of light. When the laser pulse duration is substantially shorter than the time of propagation of acoustic

waves in a medium, the profile of the induced temporal distribution of pressure in the medium reflects the profile of the spatial distribution of optical absorption by the medium [170].

The principle of operation of an optoacoustic tomograph is shown in Fig. 14. Fig. 15 shows the results of *in vivo* diagnostics of a model carcinoma of the milk gland [170]. An acoustic pulse excited by a short laser pulse absorbed by a macroscopic inhomogeneity of the tissue (tumor) was detected with a detector. The propagation velocity of the acoustic pulse and its shape give information on the type, size, and depth of the inhomogeneity position.

By detecting the time dependence of the acoustic signal excited by laser pulses, one can visualise the local pathological disorders in tissues at a depth of up to $2-3$ mm with a spatial resolution of 20 μm.

The method based on irradiation of tissues by lasers and simultaneous ultrasonic probing is also applied in medical tomography [171, 172].
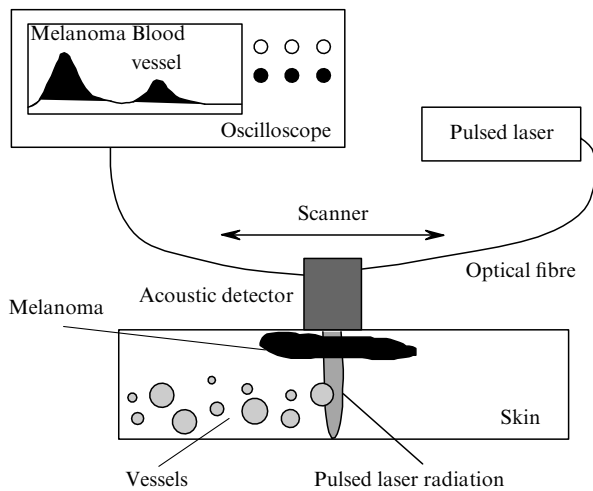
11. Methods for controlling the optical properties of tissues as applied to optical tomography

A conventional method for improving the image quality in absorption tomography is the use of contrasting agents, which are capable of accumulating in tissues. This method can be also employed in optical diffusion tomography by introducing into tissues the substances absorbing light at the wavelength of probe radiation, as well as fluorescing compounds [173 – 180].

The optical properties of tissues subjected to diagnostics can be also controlled by changing their scattering coefficient. By reducing the scattering coefficient of the main component of the tissue, inside which inhomogeneities are located, one can substantially expand the possibilities of optical tomography, especially when coherent methods are used [167, 181 – 191]. The scattering coefficient μ_s is determined by the quantity $m = n_s/n_0$ [167] (where n_s and n_0 are the refractive indices of scatterers and the environment): $\mu_s \propto (m-1)^2$. Small variations in m cause substantial variations in the scattering coefficient and the intensity of a probe beam transmitted by the object (the number of ballistic photons) [181, 183].

Typical values of the refractive indices of the components of cells and tissues in the visible and near-IR regions are $1.35-1.36$ (extracell liquid), $1.36-1.37$ (cytoplasm), 1.46 (membrane), $1.38-1.41$ (nucleus), $1.38-1.41$ (mitochondria and other organelles), 1.47 (hydrated collagen), and $1.6-1.7$ (melanin [167].

A substantial immersion bleaching of the human and animal sclera and skin was achieved in *in vitro* and *in vivo* studies by using some biologically compatible chemical agents (X-ray contrast substances based on sugars (verographine and trasograph) and glucose, glycerol, propylene glycol, etc.) [167, 181 – 186]. The immersion bleaching is especially important for optical coherent tomography, where it allows one to increase substantially the probing depth and enhance the image contrast [187 – 191]. Fig. 16 shows *in vitro* optical coherent tomography images of the human stomach tissue before and after applying the immersion agent [188]. One can see that optical immersion

Figure 14. Principal scheme of a pulsed optoacoustic tomograph [170].
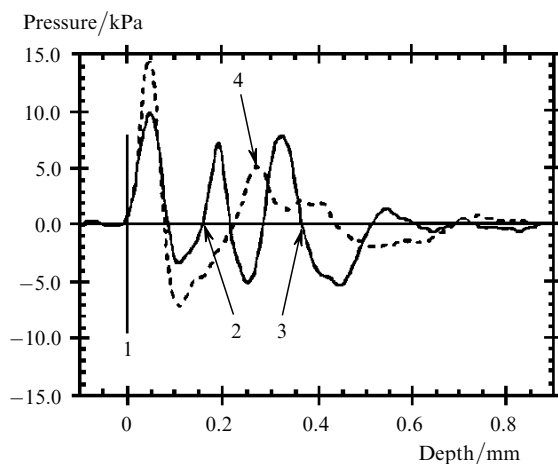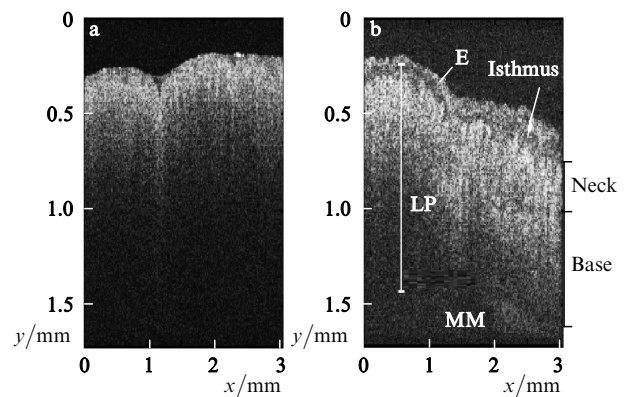
Figure 15. Optoacoustic signals measured *in vivo* for the tumor and healthy skin for a carcinoma of the milk gland of a mouse: (*1*) skin surface; (*2*) front part of tumor; (*3*) rear part of tumor; (*4*) healthy tissue [170].

Figure 16. *In vitro* optical coherent tomography images of the human stomach bottom tissue in norm (vertical axis corresponds to the transverse scan of the sample; horizontal axis corresponds to the longitudinal scan) (a) without and (b) with immersion liquid applied (80% solution of propylene glycol); E is epithelium; L is lamina propia; MM is muscular part of mucous membrane [188].

substantially increases the probing depth and enhances the image quality. The probing depth without applying propylene glycol is only 0.4 mm, whereas after its applying the probing depth achieves 1.4 mm. A substantial enhancement of the image contrast after applying glycerol on the skin is demonstrated by *in vivo* images of the rat skin in Fig. 17 [186]. The depth profiles of the optical coherent tomography signal, corresponding to images for the same point on the surface, show the appearance of new details during the action of the agent.
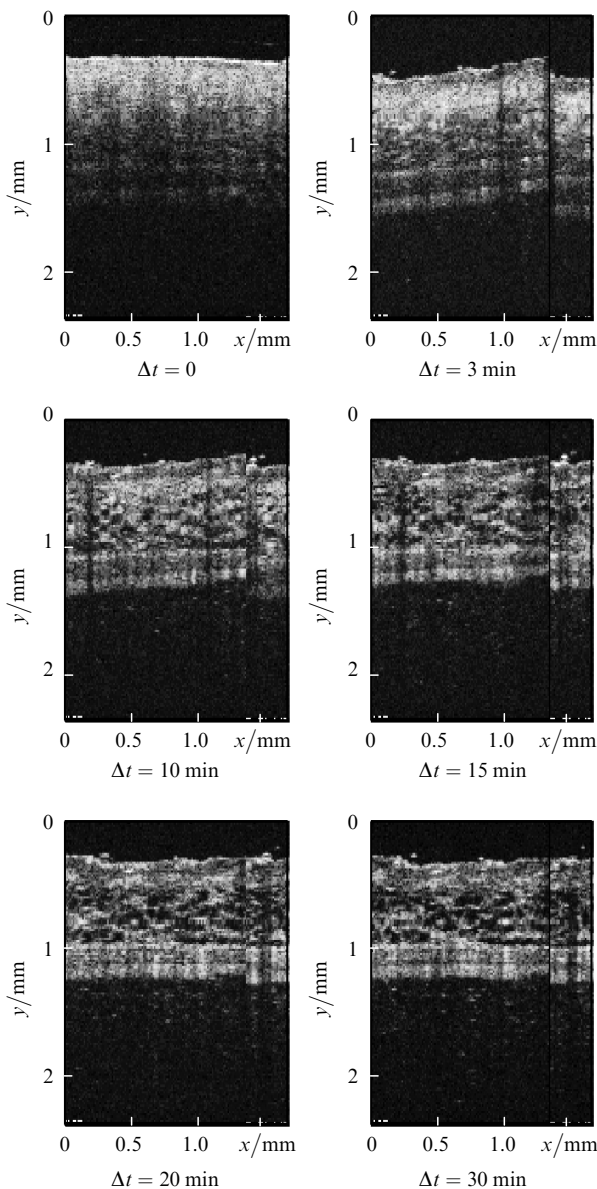
Figure 17. Dynamic *in vivo* optical coherent tomography images of the rat skin at different instants of time ($\Delta t = 0 - 30$ min) after glycerol application [186]; vertical axis – transverse scan; horizontal axis – longitudinal scan.

After injection of 40 % glucose to the skin (derma) of a volunteer, the attenuation of the optical coherent tomography signal μ_1 at a wavelength of 820 nm decreased from 1.97 to 1.21 mm^{-1} for 13 min, which corresponds to a more than twofold increase in the transmission coefficient of the tissie, $I/I_0 \exp(-\mu_t)$ [189].

The concept of immersion bleaching of a layer of moving or sedimentation blood was successfully used in the optical coherent tomography diagnostics [190, 191]. This bleaching is important for obtaining distinct images of a vessel wall (atherosclerotic plaque) through a blood layer with the help of optical coherent tomography endoscopes. Glycerol and dextran have a high efficiency in this respect [191].

12. Conclusions

The optical tomography methods used in medicine can be divided into two main groups: incoherent methods, which are used for probing tissues at depths of about several centimetres and are characterised by a relatively low spatial resolution (~ 1 mm), and coherent methods, which allow one to analyse the structure of tissues and their dynamics with a spatial resolution up to 1 μm at depths of the order of transport length, which is equal $0.5 - 1.5$ mm in tissues. Both these approaches are extensively employed in clinics, as testified by many papers devoted to diagnostic applications of various modifications of optical diffusion tomography and optical coherent tomography. A general trend in the development of optical diffusion tomography and optical coherent tomography technologies in medicine is the creation of multifunctional diagnostic systems for *in vivo* monitoring of various parameters of tissues and organs.

Optoacoustic tomography is promising for the localisation of optical inhomogeneities in comparatively thick tissues (up to 1 cm) with a spatial resolution at a level of the cell size ($20 - 50$ μm).

The method of optical immersion allows one to increase substantially (by several times) the probing depth of tissues and to enhance considerably the image quality (contrast).

References

1. Welch A.J., van Gemert M.C.J. (Eds). *Tissue Optics* (N.Y.: Academic, 1992).
2. Muller G., Chance B., Alfano R., et al. (Eds) *Medical Optical Tomography: Functional Imaging and Monitoring* (Bellingham, Washington, USA: SPIE Press, 1993) Vol. IS11.
3. Tuchin V.V. *Lazery i volokonnaya optika v biomeditsinskikh issledovaniyakh* (Lasers and Fibre Optics in Biomedical Studies) (Saratov: Izd. Saratov Univ., 1998).
4. Yaroslavsky A.N., et al., in *Handbook of Optical Medical Diagnostics*. Ed. by Tuchin V.V. (Bellingham, Washington, USA: SPIE Press, 2002) p. 369.
5. Ishimaru A. *Wave Propagation and Scattering in Randon Media* (New York: Academic Press, 1978).
6. Ishimaru A. *Trudy IIER*, **65**, 46 (1977).
7. Maret G., Wolf P.E. *Z. Phys. B*, **65**, 409 (1987).
8. MacKintosh F.C., John S. *Phys. Rev. B*, **40**, 2382 (1989).
9. Arridge S.R., Cope M., Delpy D.T. *Phys. Med. Biol.*, **37**, 1531 (1992).
10. Perelman L.T., et al. *Phys. Rev. Lett.*, **72**, 1341 (1994).
11. Bicout D., et al. *Phys. Rev. E*, **49**, 1767 (1994).
12. Zimnyakov D.A., Tuchin V.V. *Pis'ma Zh. Eksp. Teor. Fiz.*, **67**, 476 (1998).

13. Zimnyakov D.A. *Waves in Random Media*, **10**, 417 (2000).

14. Sobolev V.V. *A Treatise on Radiative Transfer* (Princeton, NJ: van Nostrand-Reinhold, 1963).

15. Hammersley J.M., Handscomb D.C. *Monte Carlo methods* (New York: J. Wiley & Sons, 1964).

16. Jacques S.L., Wang L., in *Optical-Thermal Response of Laser-Irradiated Tissue* (New York: Plenum Press, 1995) p. 73.

17. Wang L., Jacques S.L. *Med. Phys.*, **21**, 1081 (1994).

18. Vera M.U., Lemueux P.-A., Durian D.J. *J. Opt. Soc. Am.*, **14**, 2800 (1997).

19. Feng S., Zeng F., Chance B. *Proc. SPIE Int. Soc. Opt. Eng.*, **1888**, 78 (1993).

20. Yoo K.M., Liu F., Alfano R.R. *Phys. Rev. Lett.*, **54**, 2647 (1990).

21. Freund I., Kaveh M., Rosenbluh M. *Phys. Rev. Lett.*, **50**, 1130 (1988).

22. Zhu J.X., Pine D.J., Weitz D.A. *Phys. Rev. A* **44**, 3948 (1991).

23. Vera M.U., Durian D.J. *Phys. Rev. E*, **53**, 3215 (1996).

24. Haskell R.C., et al. *J. Opt. Soc. Am. A*, **11**, 2727 (1994).

25. Durduran T., et al. *J. Opt. Soc. Am. A*, **14**, 3358 (1997).

26. Furutsu K., Yamada Y. *Phys. Rev. E*, **50**, 3634 (1994).

27. Furutsu K. *J. Opt. Soc. Am. A*, **14**, 267 (1997).

28. Bassani M., et al. *Opt. Lett.*, **22**, 853 (1997).

29. Case M.C., Zweifel P.F. *Linear Transport Theory* (New York: Addison-Wesley, 1967).

30. Lemieux P.-A., Vera M.U., Durian D.J. *Phys. Rev. E*, **57**, 4498 (1998).

31. Patterson M.S., Chance B., Wilson B.C. *Appl. Opt.*, **28**, 2331 (1989).

32. Andersson-Engels S., et al. *Opt. Lett.*, **15**, 1179 (1990).

33. Hebden J.C., Kruger R.A., Wong K.S. *Appl. Opt.*, **30**, 788 (1991).

34. Das B.B., Yoo K.M., Alfano R.R. *Opt. Lett.*, **18**, 1092 (1993).

35. Lyubimov V.V. *Opt. Spektrosk.*, **76**, 814 (1994).

36. De Haller E.B. *J. Biomed. Opt.*, **1**, 7 (1996).

37. Cubeddi R., et al. *Appl. Opt.*, **35**, 4533 (1996).

38. Cai W., et al. *Proc. Natl. Acad. Sci. USA* **93**, 13561 (1996).

39. Vorob'ev N.S. et al. *Kvantovaya Elektron.*, **24**, 567 (1997) [*Quantum Electron.*, **27**, 549 (1997)].

40. Tereshchenko S.A. et al. *Kvantovaya Elektron.*, **25**, 853 (1998) [*Quantum Electron.*, **28**, 831 (1998)].

41. Vorob'ev N.S., et al. *Kvantovaya Elektron.*, **28**, 181 (1999) [*Quantum Electron.*, **29**, 737 (1999)].

42. Hyde S.C.W., et al. *Opt. Commun.*, **122**, 111 (1996).

43. Hauger C., et al. *Opt. Commun.*, **131**, 351 (1996).

44. Inaba H., in *Medical Optical Tomography: Functional Imaging and Monitoring*. Ed. by Muller G., Chance B., et al. (Bellingham, Washington, USA: SPIE Press, 1993) Vol. IS11, p. 317.

45. Schmitt J.M., Gandjbakhche A.H., Bonnar R.F. *Appl. Opt.*, **31**, 6535 (1992).

46. Demos S.G., Alfano R.R. *Opt. Lett.*, **21**, 161 (1996).

47. Wang L., et al. *Science*, **253**, 769 (1991).

48. Wang L., et al. *Opt. Lett.*, **18**, 241 (1993).

49. Wang L.M., Ho P.P., Alfano R.R. *Appl. Opt.*, **32**, 535 (1993).

50. Duncan M.C., et al. *Opt. Lett.*, **16**, 1868 (1993).

51. Mahon R., et al. *Appl. Opt.*, **18**, 7425 (1993).

52. Le Tolguenes G., Devaus F., Lantz E. *Opt. Lett.*, **24**, 1047 (1999).

53. Benaron D.A., Stevenson D.K. *Science*, **259**, 1463 (1993).

54. Eda H., et al. *Rev. Sci. Instrum.*, **70**, 3595 (1999).

55. Schmitt F.E.W., et al. *Rev. Sci. Instrum.*, **71**, 256 (2000).

56. Schweiger M., Arridge S.R., in *OSA Trends in Optics and Photonics. Advances in Optical Imaging and Photon Migration*. Ed. by Altano R.R., Fujimoto G.G. (Washington DC, USA: Optical Society of America, 1996) Vol. 2, p. 263.

57. Rodriguez J., et al. *Proc. SPIE Int. Soc. Opt. Eng.*, **3659**, 375 (1999).

58. Rodriguez J., et al., in *Handbook of Optical Medical Diagnostics*. Ed. by Tuchin V.V. (Bellingham, Washington, USA: SPIE Press, 2002) p. 357.

59. Grosenick D., et al. *Appl. Opt.*, **38**, 2927 (1999).

60. Hintz S.R., et al. *Pediatr. Res.*, **45**, 54 (1999).

61. Fantini S., Franceschini M.A., Gratton E.J. *Opt. Soc. Am. B*, **11**, 2128 (1994).

62. O'Leary M.A., et al. *Phys. Rev. Lett.*, **59**, 2658 (1992).

63. Schmitt J.M., Knuttel A., Knutson J.R. *J. Opt. Soc. Am. A*, **9**, 1832 (1992).

64. Tromberg B.J., et al. *Appl. Opt.*, **32**, 607 (1993).

65. Yodh A., Chance B. *Phys. Today*, **48**, 34 (1995).

66. Lakowicz J.R., Berndt K.W. *Chem. Phys. Lett.*, **166**, 246 (1990).

67. Berndt K.W., Lakowicz J.R. *Proc. SPIE Int. Soc. Opt. Eng.*, **1431**, 149 (1991).

68. Gratton E., et al. *Bioimaging*, **1**, 40 (1993).

69. Knuttel A., Schmitt J.M., Knutson J.R. *Appl. Opt.*, **32**, 381 (1993).

70. Sevick E.M., et al. *Appl. Opt.*, **33**, 3562 (1994).

71. Li X.D., et al. *Opt. Lett.*, **22**, 573 (1997).

72. Yao Y.Q., et al. *J. Opt. Soc. Am. A*, **14**, 325 (1997).

73. Gotz L., et al. *Akt. Radiol.*, **8**, 31 (1998).

74. Chance B., et al. *Rev. Sci. Instr.*, **69**, 3457 (1998).

75. Chance B., et al. *Rev. Sci. Instr.*, **67**, 4324 (1996).

76. Erickson M.G., Reynolds J.S., Webb K.J. *J. Opt. Soc. Am. A*, **14**, 3083 (1997).

77. Chance B., et al. *Opt. Express*, **2**, 411 (1998).

78. Fujimoto G.G., Patterson M.S. (Eds) *OSA Trends in Optics and Photonics. Advances in Optical Imaging and Photon Migration*. (Washington DC, USA: Optical Society of America, 1998) Vol. 21.

79. Chance B., et al. *OSA TOPS*, **21**, 218 (1998).

80. Chursin D.A., Shuvalov V.V., Shutov I.V. *Kvantovaya Elektron.*, **29**, 83 (1999) [*Quantum Electron.*, **29**, 921 (1999)].

81. Malikov E.V. et al. *Kvantovaya Elektron.*, **30**, 78 (2000) [*Quantum Electron.*, **30**, 78 (2000)].

82. Jarry G., et al. *J. Biomed. Eng.*, **6**, 70 (1984).

83. Jackson P.C., et al. *Brit. J. Radiol.*, **60**, 375 (1987).

84. Tamura M., Nomura Y., Hazeki O. *Rev. Laser Eng. (Jpn)*, **15**, 74 (1987).

85. Oda I., et al. *Proc. SPIE Int. Soc. Opt. Eng.*, **1431**, 284 (1991).

86. Luo Q., Nioka S., Chance B., in *OSA Trends in Optics and Photonics. Advances in Optical Imaging and Photon Migration*. Ed. by Altano R.R., Fujimoto G.G. (Washington DC, USA: Optical Society of America, 1996) Vol. 2, p. 155.

87. Luo Q., Nioka S., Chance B. *Proc. SPIE Int. Soc. Opt. Eng.*, **2979**, 84 (1997).

88. Chance B., et al. *Phil Tran. R. Soc. Lond. B*, **352**, 707 (1997).

89. Luo Q., et al., in *Handbook of Optical Medical Diagnostics*. Ed. by Tuchin V.V. (Bellingham, Washington, USA: SPIE Press, 2002) p. 455.

90. Cheng X., Boas D.A. *Opt. Express*, 3, 118 (1998).

91. Arridge S.R. *Inverse Problems*, **15**, R41 (1999).

92. Boas D.A. *OSA Trends in Optics and Photonics*, **21**, 183 (1998).

93. Markel V.A., Schotland J.C. *J. Opt. Soc. Am. A*, **18**, 1336 (2001).

94. Jong C., et al. *J. Opt. Soc. Am. A*, **16**, 2400 (1999).

95. Hielscher A.H., et al. *OSA Trends in Optics and Photonics*, **21**, 156 (1998).

96. Boas D.A., et al. *Proc. Nat. Acad. Sci. USA*, **91**, 4887 (1994).

97. Volkonskii V.B. et al. *Opt. Spektrosk.*, **86**, 253 (1999).

98. Volkonskii V.B. et al. *Opt. Spektrosk.*, **87**, 422 (1999).

99. Kravtsenyuk O.V., Lyubimov V.V. *Opt. Spektrosk.*, **39**, 107 (2000).

100. Kalintsev A.G., et al. *Proc. SPIE Int. Soc. Opt. Eng.*, **4242**, 275 (2001).

101. Tret'yakov E.V., Shuvalov V.V., Shutov I.V *Kvantovaya Elektron.*, **31**, 1095 (2001) [*Quantum Electron.*, **31**, 1095 (2001)].

102. Shuvalov V.V., et al. *Laser Phys.*, **11**, 636 (2001).

103. Arridge S.R., in *OSA Tech. digest on biomed. opt.* (Washington DC, USA: Optical Society of America, 1999) p. 206.

104. Fercher A.F., Roth E. *Proc. SPIE Int. Soc. Opt. Eng.*, **658**, 48 (1986).

105. Fercher A.F., Mengedoht K., Werner W. *Opt. Lett.*, **13**, 186 (1988).

106. Fercher A.F., et al. *Am. J. Ophtalm.*, **116**, 113 (1993).

107. Fercher A.F., et al. *Opt. Commun.*, **117**, 43 (1995).

108. Huang D., et al. *Science*, **254**, 1178 (1991).

109. Swanson E.A., et al. *Opt. Lett.*, **18**, 1864 (1993).

110. Swanson E.A., et al. *Opt. Lett.*, **17**, 151 (1992).

111. Sergeev A.M., et al. *Proc. SPIE Int. Opt. Soc. Eng.*, **2328**, 144 (1994).

112. Gelikonov V.M., et al. *Pis'ma Zh. Eksp. Teor. Fiz.*, **61**, 149 (1995).

113. Gladkova N.D., et al. *EULAR J.*, **24**, 256 (1995).

114. Sergeev A.M., et al. *Opt. Express*, **1**, 432 (1997).

115. Roper S.N., et al. *J. Neurosci. Meth.*, **80**, 91 (1998).

116. Fercher A.F. *J. Biomed. Opt.*, **1**, 157 (1996).

117. Walti R., et al. *J. Biomed. Opt.*, **3**, 253 (1998).

118. Podoleanu A.G., et al. *J. Biomed. Opt.*, **3**, 12 (1998).

119. Baumgartner A., et al. *J. Biomed. Opt.*, **3**, 45 (1998).

120. Drexler W., et al. *J. Biomed. Opt.*, **3**, 55 (1998).

121. DiCarlo C.D., et al. *J. Biomed. Opt.*, **4**, 450 (1999).

122. Drexler W., et al. *Opt. Lett.*, **24**, 1221 (1999).

123. Tearney G.J., et al. *Science*, **276**, 2037 (1997).

124. Tearney G.J., et al. *Opt. Lett.*, **21**, 543 (1996).

125. Boppart S.A., et al. *Opt. Lett.*, **22**, 1618 (1997).

126. Feldchtein F.I., et al. *Opt. Express*, **3**, 257 (1998).

127. Kamensky V., et al. *Proc. SPIE Int. Soc. Opt. Eng.*, **2981**, 94 (1997).

128. Kamensky V., et al. *J. Biomed. Opt.*, **4**, 137 (1999).

129. Sobol E.N., et al. *Proc. SPIE Int. Soc. Opt. Eng.*, **3907**, 504 (2000).

130. Boppart S.A., et al. *J. Surgical Research*, **82**, 275 (1999).

131. Pan Y., Farkas D.L. *J. Biomed. Opt.*, **3**, 44 5 (1998).

132. Schmitt J.M., Xiang S.H., Yung K.M. *J. Opt. Soc. Am.*, **15**, 2286 (1998).

133. Morgner U., et al. *Opt. Lett.*, **24**, 411 (1999).

134. Leitgeb R., et al. *Opt. Lett.*, **25**, 820 (2000).

135. Schmitt J.M., Xiang S.H. *Opt. Lett.*, **23**, 1060 (1998).

136. Park B.H., et al. *J. Biomed. Opt.*, **6**, 474 (2001).

137. Everett M.J., et al. *Proc. SPIE Int. Soc. Opt. Eng.*, **3251**, 184 (1998).

138. Hitzenberger C.K., et al. *Proc. SPIE Int. Soc. Opt. Eng.*, **4619 – 24**, (2002).

139. De Boer J.F., et al. *Opt. Express*, **3**, 212 (1998).

140. Wang X.J., Milner T.E., Nelson J.S. *Opt. Lett.*, **20**, 1337 (1995).

141. Boas D.A., Bizheva K.K., Siegel A.M. *Opt. Lett.*, **23**, 319 (1998).

142. Kolinko V.G., et al. *J. Biomed. Opt.*, **3**, 187 (1998).

143. Chen Z., et al. *Opt. Lett.*, **22**, 64 (1997).

144. Chen Z., et al. *Opt. Lett.*, **22**, 1119 (1997).

145. Zhao Y., et al. *Opt. Lett.*, **25**, 1358 (2000).

146. Zhao Y., et al. *Opt. Lett.*, **25**, 114 (2000).

147. Zhao Y., et al. *Opt. Lett.*, **27**, 98 (2002).

148. Ren H., et al. *Opt. Lett.*, **27**, 409 (2002).

149. Barton J.K., Welch A.J., Izatt J.A. *Opt. Express*, **3**, 251 (1998).

150. Hausler G., et al. *Opt. Lett.*, **21**, 1087 (1996).

151. Eigensee A., et al. *Proc. SPIE Int. Soc. Opt. Eng.*, **2925**, 169 (1996).

152. Thompson C.A., Webb K.J., Weiner A.M. *J. Opt. Soc. Am. A*, **14**, 2269 (1997).

153. Habelhand U.H.P., Blazek V., Schmitt H.J. *J. Biomed. Opt.*, **3**, 259 (1998).

154. Pine D.J., et al. *Phys. Rev. Lett.*, **60**, 1134 (1988).

155. Cummins H.Z., and Pike E.R. (Eds) *Photon Correlation and Light Beating Spectroscopy* (New York: Plenum Press, 1974; Moscow: Mir, 1978).

156. Ackerson B.J., et al. *Thermophys. and Heat Trans.*, **6**, 577 (1992).

157. Boas D.A., Campbell L.E., Yodh A.G. *Phys. Rev. Lett.*, **75**, 1855 (1995).

158. Boas D.A., Yodh A.G. *J. Opt. Soc. Am. A*, **14**, 192 (1997).

159. Fercher A.F., Briers J.D. *Opt. Commun.*, **37**, 326 (1981).

160. Briers J.D., Fercher A.F. *Proc. SPIE Int. Soc. Opt. Eng.*, **369**, 22 (1982).

161. Briers J.D., Webster S. *Opt. Commun.* **116**, 36 (1995).

162. Briers J.D., Webster S. *J. Biomed. Opt.*, **1**, 174 (1996).

163. Zimnyakov D.A., Briers J.D., Tuchin V.V., in *Handbook of Optical Medical Diagnostics*. Ed. by Tuchin V.V. (Bellingham, Washington, USA: SPIE Press, 2002) p. 987.

164. Dunn A.K., et al. *J. of Cerebral Blood Flow and Metabolizm*, **21**, 195 (2001).

165. Sadhwani A., et al. *Appl. Opt.*, **35**, 5727 (1996).

166. Braslavsky S.E., Heihoff K., in *Handbook of Organic Photochemistry*. Ed. by Scaiano J.C. (Boca Raton: CRC Press, 1989).

167. Tuchin V.V. *SPIE Tutorial Texts in Optical Engineering* (Bellingham, Washington, USA: SPIE Press, 2000) TT38.

168. Karabutov A.A., Oraevsky A.A., in *Handbook of Optical Medical Diagnostics*. Ed. by Tuchin V.V. (Bellingham, Washington, USA: SPIE Press, 2002) p. 585.

169. Sathyam U.S., Prahl S.A. *J. Biomed. Opt.*, **2**, 251 (1997).

170. Oraevsky A.A. *IEEE/LEOS Newsletter*, **10**, 17 (1996).

171. Wang L. *Photochem. Photobiol.*, **67**, 41 (1998).

172. Kempe M., et al. *J. Opt. Soc. Am. A*, **14**, 1151 (1997).

173. Ho P.P., et al. *Appl. Opt.*, **28**, 2304 (1989).

174. Khused Yu.D., et al. *Proc. SPIE Int. Soc. Opt. Eng.*, **2078**, 521 (1993).

175. Chance B., et al. *Proc. Nat. Acad. Sci. USA*, **90**, 3423 (1993).

176. Burns D.H. *Appl. Spectr.*, **48** (5), A12 (1994).

177. Podgaetsky V.M., et al. *Proc. SPIE Int. Soc. Opt. Eng.*, **2326**, 153 (1994).

178. Li X., et al. *Proc. SPIE Int. Soc. Opt. Eng.*, **2389**, 789 (1995).

179. Riefke B., et al. *Proc. SPIE Int. Soc. Opt. Eng.*, **2927**, 199 (1996).

180. Vorob'ev N.S., et al. *Kvantovaya Elektron.*, **29**, 261 (1999) [*Quantum Electron.*, **29**, 1100 (1999)].

181. Zimnyakov D.A., Maksimova I.L., Tuchin V.V. *Opt. Spektrosk.*, **88**, 1026 (2000).

182. Tuchin V.V. (Ed.) *Handbook of Optical Biomedical Diagnostics* (Bellingham, Washington, USA: SPIE Press, 2002) PM107.

183. Maksimova I.L., Zimnyakov D.A., Tuchin V.V. *Opt. Spektrosk.*, **89**, 86 (2000).

184. Tuchin V.V. et al. *Pis'ma Zh. Tekh. Fiz.*, **27**, 11 (2001).

185. Vargas G., et al. *J. Laser. Surg. Med.*, **24**, 138 (1999).

186. Wang R.K., et al. *J. Opt. Soc. Am. B*, **18**, 948 (2001).

187. Wang R.K., Elder J.B. *Laser Physics*, **12**, 611 (2002).

188. Wang R.K., Elder J.B. *Lasers in Surgery and Medicine*, **30**, 201 (2002).

189. Lakodina N.A., et al., in *OSA Trends in Optics and Photonics (TOPS)*, **73**, 550 (2002).

190. Brezinski M., et al. *Circulation*, **103**, 1999 (2001).

191. Tuchin V.V., Xu X., Wang R.K. *Appl. Opt.*, **41**, 258 (2002).